DEGRADATION OF ZnS PHOSPHORS DURING ELECTRON BEAM
BOMBARDMENT

By

Joseph Samuel Sebastian

A DISSERTATION PRESENTED TO THE GRADUATE SCHOOL OF THE
UNIVERSITY OF FLORIDA IN PARTIAL FULFILLMENT OF THE REQUIREMENTS
FOR THE DEGREE OF DOCTOR OF PHILOSOPHY

UNIVERSITY OF FLORIDA

1997

ACKNOWLEDGMENTS

First and foremost I must thank my parents Sam and Jo Ann whose love and support know no bounds. Without their encouragement and guidance I would surely never have been able to accomplish this goal.

I also owe a great deal to my advisor Dr. Paul Holloway, a man of seemingly limitless energy, who despite his hectic schedule always found time to answer my questions and keep me moving forward in my research. Dr. Hendrik Swart who visited our research group for a year from South Africa taught me a great deal about Auger (repair), and data analysis. Dr. Mark Davidson always came up with innovative ways to collect the data I needed, and humored me when I told him I needed it today. Dr. W. Brock Alexander lent his expertise for interpretation of the HRXRD results, and Dr. Maggie Puga-Lambert performed the SIMS analysis and guided me through the data reduction. Dean Evans at the University of Georgia sacrificed part of his spring break to collect the low voltage efficiency data. Dr. T.J. Kim, with whom I share an office, was always there to encourage me, offer suggestions and share the occasional cup of coffee after a long day.

Finally I would like to thank ISHM (now IMAPS) and the Phosphor Technology Center of Excellence for their continued financial support throughout my graduate career.

TABLE OF CONTENTS

DEGRADATION OF ZnS PHOSPHORS DURING ELECTRON BEAM
BOMBARDMENT

By

Joseph Samuel Sebastian

August 1997

Samples of ZnS:Mn thin films and single crystals have been subject to electron
bombardment (0.6 to 4 KeV) over a range of pressures from 1×10^{-6} to 5×10^{-8} Torr.
Various gases including hydrogen, oxygen, and water vapor were introduced into the
ambient during bombardment to assess their effects on the phosphor surface. Auger
Electron Spectroscopy data indicate that electron bombardment in the presence of O_2
and H_2O caused depletion of sulfur and accumulation of oxygen on the surface.
Hydrogen also caused depletion of sulfur. Removal of sulfur was shown to be
consistent with electron beam dissociation of molecular species to atomic hydrogen
and/or oxygen, followed by a surface reaction to form high vapor pressure sulfur
compounds (e.g., SO_x and H_2S). A model for this electron stimulated surface reaction
(ESSR) has been proposed that correlates well with the ZnS data. Concurrent increases

in the oxygen and zinc APPH during bombardment in oxygen and water vapor and postdegradation analysis with X-Ray Photoelectron Spectroscopy show the conversion of the surface of ZnS to ZnO. These changes in surface chemistry, specifically the removal of sulfur and growth of the surface oxide, are also correlated to a reduction in cathodoluminescent (CL) brightness from the samples. There are three components of the degraded phosphor that could account for this loss of CL brightness: the oxide layer, the activator ion, and the host lattice. Optical absorption of light, attenuation of the primary electron beam by the oxide layer and changes in activator ion efficiency were investigated, and these factors could account for at most 13% of the brightness loss. These results indicate the majority of the brightness loss must be caused by the host lattice, ZnS. Both the degraded and reference areas of single crystal ZnS were analyzed by Secondary Ion Mass Spectrometry, which showed significantly more oxygen in the first 51 nanometers (nm) of the degraded sample as compared to the reference. Additional thermoluminescent experiments are consistent with oxygen substitution for sulfur in the lattice to form isoelectronic electron traps. The data suggest that these non-radiative traps reduce the excitation rate of the Mn^{+2} ions, which causes reduced CL brightness.

CHAPTER I
INTRODUCTION

It is difficult to imagine how the information age would have developed without the cathode ray tube (CRT) display (Figure 1.1). Arguably, it might not have happened at all. With its humble beginnings in black and white television, the CRT has evolved into the full color high definition displays we are familiar with today. However, engineers have tried to replace the CRT, for many reasons. CRTs are large and heavy, and they are fabricated out of glass which can lead to irreparable damage during shipping and handling. Typically, they operate at 20 kilovolts (KV) or more which calls for high voltage power supplies and shielding to prevent shock hazard. Phosphor dots are patterned on the face plate of a CRT tube and an electron beam is deflected by electromagnetic fields to excite the phosphor dots line by line. There are, however, limits on the amount the electron beam can be deflected, which restricts the maximum diagonal size of a CRT display.

These and other issues have been addressed by a variety of alternate display technologies. Projection television [Hase et al. 1990] allows large display areas by projecting the images from three CRT displays (red, green, and blue) onto a larger screen for viewing. Plasma displays [Mikoshiba 1993] use, as the name suggests, a plasma discharge to excite luminescence in the phosphors. Inexpensive displays for dashboards and consumer electronics are often of the vacuum fluorescent display (VFD)

1

type [Morimoto 1982]. Their familiar blue glow comes from the ZnO:Zn phosphor commonly used because of its long life and high brightness. Electroluminescent (EL) displays [Holloway et al. 1994] first in monochrome yellow and recently in full color, provide a very rugged, solid-state, although expensive display. These technologies have provided solutions for many display applications, but they have failed to address one of the largest and most rapidly expanding areas.

Technological advances in computer power and compactness have fueled development of new display technologies. For the notebook computer to become a reality large area, thin, lightweight displays were required. In addition, to allow for sufficient battery life, the power consumption had to be controlled. It was under these demanding conditions that liquid crystal displays (LCDs) [Doane 1995] emerged as the technology of choice. LCD technology has developed from monochrome to full color, and are now available in sizes comparable to 14" diagonal CRT computer monitors. Early problems with line addressed or passive LCDs were eliminated by the introduction of the thin film transistor (TFT) or active matrix LCD (AMLCD) [Brody 1973]. In this design each pixel is individually addressed by its own switching transistor. These advances have led to the dominance of the LCD in portable computer design, with more than a 95% market share worldwide.

While the TFT-LCD provides good color rendering and eliminates the ghosting found in passive LCDs, it suffers from several major drawbacks. First, it is enormously complex to manufacture, typically requiring more than 150 separate process steps (Figure 1.2) which leads to low production yields and high cost [Matsueda 1989, Nakajima 1989]. Second, it suffers from slow refresh rates which makes it unsuitable

for high resolution full motion video. Third, the LCD is a light valve which filters light passing through it from a white light source located behind the panel. This limits the power efficiency of the display, because much of the light intensity from the back light is lost when it passes through the LCD panel. Obtaining sufficient viewing contrast and brightness in direct sunlight with this type of display is difficult. Finally, LCDs tend to be fragile, because they are patterned on thin glass substrates and are sensitive to temperature variations which drastically alter the display's contrast, both attributes limit their service environment. These limitations have provided incentives for the development of competing display technologies.

Of these emerging technologies, the field emission display (FED) [Curtin 1991] (Figure 1.3) is projected to be the most likely to replace the LCD (Table 1.1). In a FED much as in a CRT phosphor dots deposited by electrophoresis are patterned on a glass face plate that has been coated with a clear conductive layer (ITO). This face plate is supported above the base plate by insulating spacers positioned periodically between the phosphor dots. The back plate, which is typically insulating, is patterned with metal lines that serve as the row electrodes for addressing the individual pixels. Emitter tips are deposited [Spindt 1968] on the row electrodes and an insulating layer is deposited around these tips. The column electrodes are deposited on top of this structure and individual pixels are addressed by applying current to the appropriate row and column electrodes. Under high electric fields (i.e., 10^6 V/cm) electrons are emitted from these tips and excite luminescence from the phosphors.

Both the power consumption and thickness of CRTs can be reduced by utilizing multiple electron emitters per pixel, as opposed to a single scanned electron gun. This

approach is utilized in the FED and each display pixel has many (tens to thousands) atomically sharp emitter tips. For better portability and reduced cost, it is desirable to lower the electron beam voltage in the FED to less than 500 volts. Under these conditions, the challenge has been to achieve a phosphor with acceptable efficiency, conductivity, brightness, and lifetime.

A phosphor can be thought of as a luminescent ion which is embedded in a host material. When this material is bombarded with an electron beam it gives off light and this process is called cathodoluminescence or CL.. The brightness of the cathodoluminescence from the phosphor is proportional to the power applied [Ozawa 1990]. The power (P) available in an electron beam is equal to the voltage (V) times the current (I) ($P = V \times I$). When the voltage of the electron beam exceeds the threshold (minimum) voltage necessary to excite the activators in the phosphor, the phosphor will luminesce. As the voltage is increased well above the bandgap of the host lattice, a single incoming electron may create many electron-hole pairs along its path before its energy is reduced below the luminescent threshold voltage. As a result, most phosphors are bombarded by electrons whose energies are well above the threshold energies, so each incoming electron produces a very large number of electrons and holes in the conduction and valence bands, resulting in improved brightness.

To retain brightness at low voltage, the power level must be maintained and therefore the beam current must be increased as the voltage is reduced. There is, however, a limit to the amount of current a phosphor can withstand before the onset of saturation (reduction of the incremental increase in light output for an incremental increase in power) and degradation (loss of brightness at constant power). In addition,

at low energies (< 500 eV) the electrons penetrate only a few tens of nanometers before their energy is reduced by inelastic scattering, to below the threshold required for luminescence. Since the penetration of electrons into the phosphor is short, the majority of luminescence is expected to originate near the surface, and any attempts to understand the degradation or improve phosphor lifetimes must concentrate on this region.

Sulfide-based phosphors, which have been used for some time in CRTs, are currently being studied for use in FEDs. This class of phosphors was chosen for their high efficiencies and high brightness, and they have demonstrated acceptable lifetimes when excited at 20 keV or more. However, ZnS-based low voltage (primary beam energies of 2 keV or less) FEDs have exhibited lifetimes of only about 200 C/cm^2 [Itoh et al. 1989, Petrovich 1995]. The characteristics of these failures are reduced luminescent brightness (less than 50% of the original brightness) at high coulombic (e.g., 200 C/cm^2) loadings [Sebastian et al. 1997]. Because low energy electrons (i.e., less than 500 eV), have a range of only a few nanometers (nm) in ZnS [Swart et al. 1997], the phosphor material near the surface is critical to the low voltage cathodoluminescence of the material. The objective of this study is therefore to better understand the degradation mechanisms that occur during electron beam bombardment of phosphor materials. This information should lead to better performance and longer life of ZnS phosphors for use in FEDs.

In order to study the surface and near surface region of the phosphor a chemical analysis technique which would sample this region without influence from the bulk material was required. Auger electron spectroscopy was chosen because it typically

only samples the first few nanometers of the sample [Holloway 1980]. In addition the same primary electron beam that is used to excite the sample for Auger analysis also causes luminescence, allowing the simultaneous collection of cathodoluminescent information. Auger electron spectroscopy data indicate that electron bombardment in the presence of O_2 and H_2O caused depletion of sulfur and formation of an oxide layer on the surface. These changes in surface chemistry are also correlated to a reduction in cathodoluminescent (CL) brightness from the samples. Although there are three components of the degraded phosphor that could account for this loss of CL brightness the oxide layer, activator ion and the host lattice, the results indicate the majority of the brightness loss must be caused by the host lattice, ZnS. In the chapters that follow, these results are discussed in some detail, and a model of the electron stimulated surface reaction (ESSR) is developed based on these observations.

Table 1.1.   A comparison of FED and AMLCD characteristics.

	FED	TFT-LCD
Thickness	6-10 mm	23 mm
Weight	<0.20 kg	0.33 kg
Contrast ratio	>100:1	60:1 to 100:1
Viewing angle	>80^0	45^0 H, 30^0 V
Maximum brightness	>200 cd/m^2	60 cd/m^2
Power consumption at 60 cd/m^2	<1W	4W
Operating temperature	-50^0 to +80^{0}C	0^0 to 50^{0}C
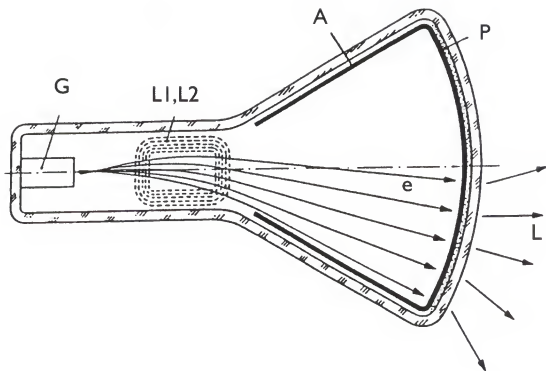
Figure 1.1.   Schematic of the cathode ray tube (CRT). Electrons (e) leaving the electron gun (G) are deflected by the magnetic fields L1 and L2, and excite the luminescent material P. A is the anode and L the emitted light [Blasse and Grabmaier 1994].

Viewing Direction

Depolarizer
Polarizer / Analyzing
Glass and Protective Coating
RGB Filter
Top ITO
Alignment Layer
Liquid Crystals
Active Matrix Structure (6 Layers)
Bottom ITO
Glass
Polarizer
Light Diffuser and UV Filter
Heater
Back Light Source

Figure 1.2.   Cross section of a typical TFT-LCD construction.

Figure 1.3.   Cross section of a field emission display (FED) [Curtin 1991].

CHAPTER 2
REVIEW OF THE LITERATURE

Luminescence

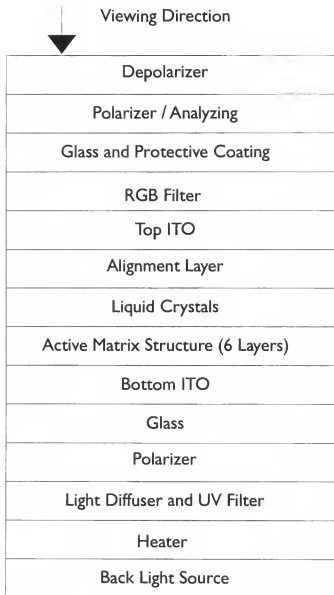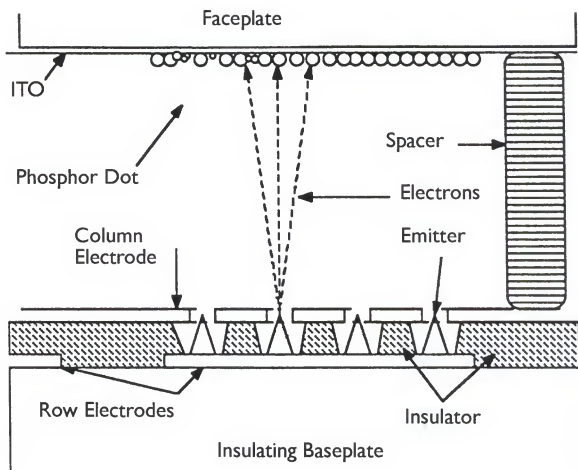The basis of most phosphors is an insulating host material which is doped with a small quantity of an impurity atom. The additional atoms may occupy interstitial or substitutional sites within the host crystal. The energy states of the electrons in the crystal originate from the energy levels of the isolated atoms. However due to the effect of the surrounding ions in the crystal, these discrete levels are broadened into energy bands [Pankove 1971]. In an insulator the lower or valence band is completely filled and the upper or conduction band is empty. Between these bands is an area of forbidden energy referred to as the bandgap, and the energy value (Eg) of this gap is a fundamental property of the crystal. Impurity atoms or lattice defects can give rise to localized electronic states within the bandgap. An electron which is excited into the conduction band (CB) may fall into these levels in the bandgap and become localized (Figure 2.1). Some time later, it may recombine with a hole and return to the ground state, or another bandgap state close to the valence band (VB), releasing energy in the process. The amount of energy released will be determined by the energy difference (ΔE) between the bandgap state and the top of the valence band (IV), bottom of the conduction band and the bandgap state (II), or between two bandgap states (III). If the

11

level is created by a nonluminescent lattice defect (I), the electron will typically return to the ground state nonradiatively, transferring its energy to the lattice as a phonon, and be dissipated as heat in the host crystal. If the level is formed by a luminescent dopant however, the energy may be released as a photon of light with a wavelength corresponding to the energy difference between the dopant level and the ground state (Figure 2.1). This simple model predicts that the emission from the material would be a sharp line at a specific wavelength or series of wavelengths. While some systems (namely rare earth doped phosphors) exhibit such spectra, many phosphor systems emit in a broad band about a central wavelength. To account for this discrepancy a more sophisticated model is required, one which takes into consideration the effects of the host lattice on the luminescent center.

Configurational Coordinate Model

The shape of an optical emission band can be explained by using the configurational coordinate diagram [Blasse and Grabmaier 1994]. This diagram illustrates the potential energy curves of the system as a function of a configurational coordinate, which describes one of the vibrational modes of the luminescent center. This model has been investigated in some detail [Hernderson and Imbusch 1989, Di Bartolo 1968] and for clarity only the symmetrical stretching or breathing mode will be discussed here. In this vibrational (phonon) mode the surrounding ligands move in phase away from and toward a central metal ion at rest (Figure 2.2).

The configurational coordinate diagram for this mode reduces to a plot of energy E versus the metal ligand distance R, as shown in figure 2.3 [Blasse and Grabmaier 1994]. This simplification neglects all other vibrational modes which might cause distortions in the excited state, which are nonetheless important and will be discussed later. If the vibrations in this model are assumed to be harmonic then the restoring force F will be proportional to the displacement R

$$F = -k(R - R_O) \qquad (2.1)$$

where k is the force constant of the oscillator. This type of force corresponds to a potential energy function with a parabolic dependence on the displacement distance R

$$E = \frac{1}{2}k(R - R_O)^2 \qquad (2.2)$$

and the minimum (R_o) of the parabola corresponds to the equilibrium position in the ground state. The quantum mechanical solution for this type of harmonic oscillator gives discrete energy levels of the oscillator

$$E_a = (a + \frac{1}{2})h\upsilon \qquad (2.3)$$

where a=0,1,2,... and υ is the frequency of the oscillator [Atkins 1990]. This relationship holds true for both the ground and excited states of the system. However, because there are differences in the chemical bonding of these two states, the parabolas for the

excited and ground states have different values of the equilibrium distance (R_o' and R_o) and force constants (k' and k). This difference is shown in figure 2.3 where the minima of the parabolas are shifted relative to each other by a distance ΔR [Blasse and Grabmaier 1994] where

$$\Delta R = R_O' - R_O. \qquad (2.4)$$

Transitions between the parabola are electronic transitions and since the electrons move much faster than the ions, the electronic transition takes place in essentially static surroundings [Hummel 1985] which implies a vertical transition. After this transition the luminescent center will be in a high (a>0) vibrational level of the excited state. Before the center can return to the ground state it must give up excess energy to the surroundings and return to the lowest level of the excited state. Because changes in the diagram along the R axis are nuclear, indicating a change in the equilibrium interatomic distance, another way to describe this process is to say that the nuclei adjust their positions to the excited state, so that the new interatomic distances are the equilibrium distances of the excited state. The configurational coordinate for the equilibrium position of the excited state changes from Ro to R'o, and this process is called relaxation.

The lowest vibrational level (a'=0) of the excited state in not a point at the apex of the parabola but rather a level of finite width near the bottom of the well (Figure 2.3). The electrons are distributed within this level according to a quantum mechanical probability function (Figure 2.4) [Hummel 1985]. Radiative transitions can

therefore occur from any point on this level and the emission will be in a band. The distribution of wavelengths and intensities within the band is determined by the distribution of electrons over the lowest excited level, and the relative shapes of the parabolas representing the ground and excited states. In addition, the configurational coordinate model assumes that the surroundings and symmetry of all the luminescent centers are the same. But centers near defects or surfaces experience covalency and crystal fields slightly different from those in the bulk, which results in additional (inhomogeneous) broadening of the emission peak [Blasse and Grabmaier 1994].

Once the center is in the lowest excited vibrational state it can spontaneously emit radiation and return to the ground state. However, not every transition between the ground and excited states can occur as an optical transition, because these transitions are governed by selection rules. The most important selection rules are spin selection, which forbids electronic transitions between levels with different spin states and the parity selection rule which forbids electronic (electric-dipole) transitions between levels with the same parity [Henderson and Imbusch 1989]. Forbidden transitions can however occur when the selection rules are relaxed by the asymmetry of the crystal field caused by other vibrational modes in the host lattice [Cotton 1990], although the probability of these transitions is low which leaves the center in the excited state for a comparatively long time. The longer the center remains in the excited state the higher the probability that it will undergo a non-radiative transition.

Energy Flow in the Phosphor

A phosphor can be envisioned as a host lattice into which activator ions are embedded. When a high energy electron passes through the phosphor material, it is scattered by ionization and phonon emission producing a cascade of electron-hole pairs [Robbins 1980]. The quantum efficiency for the transfer of energy from electron-hole pairs to activator ions is called the transfer efficiency, n_t [Klaassen and Leeuw 1987]. In addition to exciting activator ions, the electrons and holes can also be captured by competing lattice imperfections, surface states, impurity related centers and other defects. In general energy transfer to these defect centers leads to nonradiaitive recombination without excitation of a luminescent center, and therefore they are often referred to as "killer centers".

Excited activator ions will decay to the ground state by both radiative and nonradiative transitions. If the decay of the luminescence is exponential with time then the total lifetime of the activator ion in the excited state, t, is given by

$$t^{-1} = t_r^{-1} + t_{nr}^{-1} \tag{2.5}$$

[Klaassen and Leeuw 1987] where t_r and t_{nr} are the radiative and non-radiative lifetimes respectively. The quantum efficiency of the luminescent process in the activator ion, often referred to as the activator efficiency, is then given by,

$$n_{act} = \frac{t_r^{-1}}{t_r^{-1} + t_{nr}^{-1}} = \frac{t}{t_r} . \tag{2.6}$$

The external radiant efficiency is defined as the ratio of the light generated to the power applied to the phosphor. At low excitation densities, where saturation effects are not significant, the external radiant efficiency n_{cr}, is given by

$$n_{cr} = \frac{E}{\epsilon} n_t n_{act} C_{ext} \qquad (2.7)$$

[Leeuw and Hooft 1983] where ϵ is the average energy to create an electron-hole pair [Robbins 1980], E is the average energy of an emitted photon, and n_t is the transfer efficiency. The average photon escape probability, C_{ext} accounts for the self-absorption of the luminescence and is the ratio of the number of photons emitted from the sample and the total number of photons generated. This assumes that all the power, apart from a correction to account for back scattered electrons based on the weighted mean atomic number [Garlick 1960], is absorbed in the phosphor and that changes in the back scatter correction due to prolonged CL excitation are small.

According to Klaassen and Leeuw [1987], the deterioration of the external efficiency of phosphor materials is due to changes to one or more of the parameters appearing in equation 2.7. Changes in the average energy to create an electron-hole pair are unlikely, and the average energy (wavelength) of the emitted photons, E, can be directly measured. Changes in the average photon escape probability, activator, and transfer efficiency must therefore be considered. A change in the refractive index and/or the absorption coefficient of the material can considerably alter the average photon escape probability. Although these two material parameters should also affect the reflection of the phosphor sample, it is nontrivial to give an explicit correlation

between the reflection coefficient and the photon escape probability. However, absorption of the light by a non luminescent layer on the surface of the phosphor would be measurable if the nature of the surface layer were known. Such a layer could be formed by cracking of molecular species (e.g., CH_4) in the residual vacuum gas. Once it was identified, the effects of this layer could be calculated and accounted for in equation 2.7.

Degradation effects may also be due to a decreased nonradiative lifetime of the activator ions in the excited state. This leads to a decreased total lifetime (equation 2.5) and consequently to a decreased activator efficiency (equation 2.6). Changes in the activator efficiency can be monitored by measuring the decay of the luminescence with time, which gives the total lifetime t. If the relative change in efficiency is equal to the relative change in total lifetime, then the degradation of the phosphor is due to a decreased activator efficiency. However if the change in brightness is larger than the relative change in total lifetime, assuming no change in the photon escape probability, then a decrease in the transfer efficiency must also be occurring. Such a decrease can, in general, be attributed to an increased energy loss in the host lattice. This increased energy loss is most often associated with an increase in the concentration of nonradiative recombination centers, which can reduce the total efficiency by reducing the transfer efficiency which causes reduction in the rate of luminescent center excitation.

Cathodoluminescence

The penetration depth of the primary electrons during cathodoluminescence is strongly dependent on their energy. In general at low energies (10 keV or less) the relationship between range (R) and energy (E) of the electron beam has the form

$$R = bE^n \qquad (2.8)$$

where b and n are related according to the expression

$$b = 250A / \rho Z^{n/2} \qquad (2.9)$$

[Feldman 1960] where ρ is the bulk density, A is the atomic or molecular weight of the material and Z is the atomic number or the number of electrons per molecule in the case of compounds. By comparison of theory to experimental results, Feldman also determined that

$$n = \frac{1.2}{(1-0.29\log_{10}Z)} \qquad (2.10)$$

By substituting b into equation 2.8, the range-energy equation becomes

$$R = 250(\frac{A}{\rho})(\frac{E}{Z^{1/2}})^n \qquad (2.11)$$

where n has the value established in equation 2.10. However, due to electron straggle the range-energy relation can not generally be used to obtain the stopping power of the material [Wang 1950]. Analysis of experiments on the transmission of electrons through thin films [Makhov 1961], demonstrated that the power delivered by the electron beam per unit area at a depth x could be approximated by

$$P(x, j_O, V_O) = j_O V_O \exp(-X^2 - X^{0.9}) \qquad (2.12)$$

where X is a normalized depth given by

$$X(x, V_O) = \frac{x}{\rho^{-1} C V_o^m} = \frac{x}{R} \qquad (2.13)$$

where x is the depth in the phosphor material, j_o is the beam current density at the surface, and V_o is the accelerating potential. C and m are characteristics of the material and Markov derived the values of these constants for many materials. This work was later applied to ZnS [Kingsley and Prener 1972] and the following range-voltage relationship was derived;

$$R(V_O) = 0.01155 V_O^{1.65} \ (microns) \qquad (2.14)$$

which predicts the penetration depth (range) of the primary electron beam based on its voltage. For ZnS the ultimate range, or the range in the solid where the relative power (P/Po) of the primary electron beam is zero [Spencer 1955], is nearly equal to twice the

Makhov range as defined in equations 2.13 and 2.14. Both the ultimate (2R) and Makhov (R) ranges are plotted in figure 2.5 as the relative power vs. distance into the solid in microns. For the purposes of modeling the CL brightness from ZnS phosphors, experimental evidence has shown that the use of Makhov's empirical relationship more accurately predicts the experimental brightness versus voltage results [Kingsley and Prener 1972].

A plot of cathodoluminescent brightness (L(V)) vs. accelerating voltage (V) when adjusted for a constant bombarding current (Figure 2.6), will yield a linear curve with a nonlinear tail at low voltages. The intercept of the linear portion of the curve with the voltage scale is often referred to as the dead voltage, V_d [Bril 1954, Bril and Klasens 1952]. Although the value of V_d differs slightly, this curve is typical [Gergely 1960] for many phosphor systems including both the bandgap (i.e., ZnS:Ag) and rare earth (i.e., Y_2O_3:Eu) type phosphors. This behavior has been explained by the existence of a dead layer [Dowling and Sewell 1953] on the surface of the phosphor. Recombination in this surface layer is dominated by surface states which are generally non-radiative defects. In addition photoconductivity measurements have been used to determine the surface recombination velocity on silicon [Benny and Morten 1958, Harten 1959] and this velocity is significantly faster than that of the luminescent centers.

In general ZnS type phosphors follow a power law decay of brightness vs. time, but a linear approximation may be utilized if the excitation density is low and the number of excited luminescent centers is low compared with the total number of dopant atoms [Schon 1954, Klasens 1958]. This approach has been successfully applied

to other phosphor systems including CdS [Auth and Ridder 1957, Broser and Broser 1958, Diemer et al. 1958].

Under these conditions, cathodoluminescent brightness L(V) can be given by

$$L(V) = \eta_O P_O \{ 1 - Q \frac{1-\exp(-BR)}{BR} \} \qquad (2.15)$$

[Gergely 1960] where R is the electron range at the primary beam voltage, B is an experimental fitting parameter, and Po is the incident power. Furthermore,

$$Q = \frac{S}{DB+S} \ and \ \eta_O = \frac{E_e}{\in} \qquad (2.16)$$

where S is the surface recombination velocity, D is the diffusion coefficient of the carriers, E_e is the average energy of emitted photons, Q is a surface recombination loss parameter (Figure 2.7), B = 1/L, and L is the ambipolar diffusion length determined by the diffusion of minority carriers [Auth and Ridder 1957]. $\in$ is the average work done to create electron hole pairs which is usually calculated by

$$\Delta \in = 3E_g. \qquad (2.17)$$

[Klein 1968]. Using data for ZnS [Feldman 1960] figure 2.8 compares the brightness vs. voltage predictions of equation 2.15 for various values of the surface recombination loss parameter, Q, with the experimental data denoted by circles. For Q=0 or no surface recombination a linear voltage vs. brightness line is predicted by the model. However,

once surface recombination is included in the model, a Q value between 0.5 and 0.6 (cm^2-sec) closely predicts the experimental results. This result indicates the importance of the surface and near surface region to the brightness obtained during low voltage (<5 keV) excitation. Factors that would influence Q such as the number and distribution of non-radiative centers (e.g., crystalline quality, defect density) would therefore be expected to have a significant influence on the brightness observed at low primary beam voltages.

ZnS:Mn Luminescence

Mn has been used for some time in ZnS to form a bright and efficient yellow phosphor material, with a broad band emission centered at 580 nm, whose breadth at high temperatures (Figure 2.9) results from the action of phonons previously discussed. However, the Mn^{+2} ion can emit light from green to orange-red depending on the strength of the crystal field of the host lattice [Blasse and Grabamier 1994]. The d^5 Tanabe-Sugano diagram in figure 2.10 is a plot of energy vs. crystal field for atoms with the d^5 configuration. At the left side of the plot, the crystal field is zero which corresponds to a free atom. For the free ion, the levels are marked $^{2S+1}$L where S is the total spin quantum number, L is the total orbital angular momentum (s=0, p=1, d=2, f=3 and g=4), and the degeneracy of these levels in the free ion is 2L+1. Because the maximum degeneracy allowed in a crystal is 3, orbitals with higher (>3) degeneracy must split into several levels when the atom is in a crystal field [Cotton 1990]. These levels in the crystal field are designated by $^{2S+1}$(A,E orT) where A signifies no

degeneracy, E is twofold, and T is threefold degeneracy. The emission in Mn occurs between the $^4T_1$ (lowest excited level) and $^6A_1$ (ground level) which is coincident with the x axis [Blasse and Grabmaier 1994]. This transition is spin forbidden, which gives the Mn^{+2} ion long decay times on the order of 1 millisecond. The different slopes of these two energy levels yields a large change in energy for small changes in crystal field, which is why Mn^{+2} emits at different colors depending on the host material. Each material presents a different set of bonding atoms to the Mn ion which produces a different crystal field and changes the energy gap between the two levels. In addition, because the crystal field in a given host is dominated (95%) by the first 4 nearest neighbors [Cotton 1990], any change in these atoms around the Mn ion will be indicated by a shift in the luminescent spectrum.

<u>Phosphor Degradation</u>

One theory that characterized phosphor degradation is the Coulomb Law which asserts that degradation of phosphor brightness at a given primary beam voltage is a function of the total charge dose deposited. In general, the ageing data for phosphors can be described by

$$I = \frac{I_o}{1 + \frac{Q}{Q_{50}}} \qquad (2.18)$$

[Pfhanl 1961] where I is the intensity, I_o is the initial intensity, Q is the charge dose in C/cm^2 (C is a Coulomb or amp-sec), and Q_{50} is the charge dose necessary to reduce the initial brightness of the phosphor by half.

Several inconsistencies during the beginning of degradation were noted in more recent experiments [Swart et al. 1997] with ZnS:Cu,Al,Ag (P22G) phosphor powders. Figure 2.11 shows the brightness of the P22G phosphor as a function of coulombic dose for several residual gas pressures. The behavior of the area of the curve labeled A was attributed to charging of the phosphor surface. The brightness in region B was stable, and this was attributed to the removal of adventitious carbon from the surface of the phosphor. The characteristic loss of brightness does not occur until C. To account for this equation 2.18 was modified as follows

$$I = \frac{I_o}{1+\frac{t'}{t'_{50}}} \qquad (2.19)$$

where $t' = t\text{-}t_c$, $t'_{50} = t'_{50}\text{-}t_c$ and t_c is the electron dose where the CL intensity begins to drop after the carbon has left the surface. Swart et al. were able to fit the degradation they observed with this modification (Figure 2.12), and determine the relative constants for equation 2.19. Furthermore Swart et al. were able to calculate the burning parameter C in Pfahnl's law [Pfahnl 1961] which is given as

$$I = \frac{I_o}{(1+CN)} \qquad (2.20)$$

where I and I_o and are the aged and initial intensities of the phosphor respectively, and N is the number of electrons deposited per cm^2. They also demonstrated the direct dependence of C on the background gas pressure. Swart observed an increase in the rate of degradation as the background gas pressure was increased. Pfahnl also noted the dependence of aging on the background gas pressure (Figure 2.13), and avoided rapid ageing of the phosphors by using screens which were sealed and maintained at high vacuum (>10^{-7} Torr).

While these simple curve fits to the brightness of a phosphor predicts the useful life of a display, it does little to illuminate the mechanism of the degradation. A better understanding of the processes leading to brightness loss in these material is therefore necessary if their lifetimes are to be improved. Some of the early work on brightness loss in phosphors [Smith and Turkevich 1954] demonstrated deterioration of ZnS after neutron irradiation. The high energy of the neutron beam caused the displacement of both Zn and S from their lattice sites and other lattice damage which made identification of the exact cause of the brightness loss difficult to determine.

Experiments that followed utilized electron beams to excite the phosphor, without excessive lattice damage. These investigations [Bryant and Hamid 1970] showed that the primary beam energy had to be at least 235 keV to displace Zn atoms and 190 keV to displace sulfur atoms. Further research showed that the 0.83 um emission from ZnS was due to sulfur vacancies, and that the emission could be reduced by annealing [Bryand and Manning 1972]. This loss of intensity of the 0.83 um peak was attributed to recovery from the electron beam induced damage during annealing.

Figure 2.14 shows the results of an isochronal annealing procedure performed on a ZnS sample irradiated by 190 keV electrons. The luminescence measured in this figure is an emission from the sulfur vacancy in the lattice, and the brightness of the emission is roughly proportional to the number of luminescent centers. Recovery of the lattice damage begins at 40^0 C and is completed at 140^0 C, demonstrating that sulfur displacement can be annealed out at relatively low temperatures. This behavior was consistent with similar photoluminescent results [Leutwein et al. 1967] and both sets of investigators associated the emission band with sulfur vacancies, and demonstrated that these vacancies affected the brightness of cathodoluminescence from ZnS.

Under the influence of the electron beam, sulfur has also been shown to enter into chemical reactions on the surface of the phosphor. $ZnSO_4$ has been shown by XPS [Itoh et al. 1989] to form during irradiation in an H_2O environment. Electron beam assisted surface chemical changes are not limited to sulfur desorption. Organic binders used for screening CRT powder phosphors have been shown to break down and release gasses into the vacuum ambient during CRT operation [Wu et al. 1982], which contribute to failure of the cathode. Electron bombardment of soda lime silica glass can form sodium-oxygen ion pairs at the surface by bond breaking [Hughes 1969]. Oxygen ions may trap a hole in the nonbonding $2p$ orbital and the sodium is then no longer rigidly bound to the oxygen [Tomozawa and Doremus 1979], and is more susceptible to desorption or field enhanced diffusion into the bulk [Ohuchi and Holloway 1982]. This diffusion has been associated with the browning of glass in CRTs [Ozawa 1990] which contributes to the loss of observed brightness. However, none of these results

provides any clear understanding of the mechanisms which lead to the loss of brightness from the ZnS phosphor itself.

Theory of Isoelectronic Traps

Isoelectronic impurities are atoms with a different atomic number but the same valence electronic configuration as the atoms they substitute for in the lattice, producing a neutral system. However, the core configuration of the host atom is necessarily different from that of the substituted atom. This difference can give rise to highly localized impurity states in the bandgap, near the band edges, which can be responsible for significant changes in both the optical and electronic properties of the host material. These changes were first reported in 1965 [Thomas et al. 1965, Aten et al. 1965] and were identified as the mechanism for unexplained optical transitions in GaP. Both of these sets of authors suggested that isoelectronic traps were important because of their high recombination efficiency, and their ability to produce trap levels relatively deep in the forbidden band of semiconductors.

Although isoelectronic impurities can be identified with transport measurements because they scatter free carriers and lower the carrier mobility, most of the experimental work has concentrated on optical spectroscopy. Measurement of both absorption and emission spectra have provided more direct information about the impurities. Many systems have been investigated including GaP:Bi [Trumbore et al. 1966], GaP:N [Thomas et al. 1965], ZnTe:O [Hopefield et al. 1966] and ZnS:Te [Baldereschi 1973]. These investigations have shown that both large and small atoms

can modify the host crystal and produce the strong impurity potential which is necessary to bind a free carrier. A significant portion of the of the ability of an isoelectronic impurity to capture carriers arises from lattice relaxation due to the size differences between the host atom and the impurity. Since the substitutional atom does not fit exactly into the vacancy site of the host atom it replaces, the displacement of surrounding atoms must be considered [Phillips 1969]. In general, lattice relaxation will increase the effectiveness of the impurities as either an electron or hole trap, and this relaxation must be taken into account to accurately predict the impurity potential (Figure 2.15) [Baldereschi 1973].

Consider that the strength of a covalent bond is inversely proportional to its length. If the impurity atom is larger than the host atom it replaces, the lattice will tend to expand around it. The elongated covalent bonds will be weaker, and therefore more attractive to holes. Similarly, the lattice will contract around a smaller impurity, increasing the bond strength and attracting electrons. Generally the displacement of the nearest neighbors can be expected to be no larger than the covalent radii difference [Vechten and Phillips 1970]. It is difficult to determine the additional attraction of carriers to the impurity site due to the lattice effects. This problem can be simplified by looking at the limit of the maximum relaxation [Baldereschi and Hopefield 1972]. At this limit, the crystal pseudopotentials are used to obtain the impurity potentials, and then take into account only the portion of the potential which is contained within the unit cell surrounding the impurity atom. If the assumption is made that only the outer electrons are modified in the bonding of the crystal, then the isoelectronic impurity potential will be the difference between the

potential of the impurity and that of the host atom it replaces.

Isoelectronic systems can be further categorized into acceptors and donors for impurities that attracted electrons or holes, respectively. In the case of isoelectronic acceptors, an electron from the conduction band is attracted to the impurity by the lattice strain field, and becomes trapped on it. This reduces the free energy of the lattice by producing a larger isoelectronic ion. The charged impurity is then attractive to holes in the valence band which recombine on the impurity atom. Because the impurity is part of the host crystal, the energy of the electron-hole recombination is efficiently coupled to the lattice and lost as heat. In general, experimental evidence has led to the following electronegativity rule [Hopfield et al. 1966]; an isoelectronic impurity will trap an electron when its electronegativity is larger than that of the matrix atom it replaces, and a hole when its electronegativity is smaller. In addition to this experimental evidence, quantum mechanical arguments have also been used to explain the effects of isoelectronic substitutions.

Allen [Allen 1971] was the first to demonstrate that relativistic spin orbital coupling effects can modify the impurity potential. These effects are however negligible for wave functions that are symmetric. In addition because the spin orbit coupling constant scales with the atomic weight of the atom, significant relativistic effects would only be expected if the impurity atom is much larger than the host atom. In most AB type semiconductors the isoelectronic impurity ground state will be predominantly p like if it is associated with the valence band and similarly s like if associated with the conduction band [Baldereschi 1973]. Taking into account this simplification, the impurity potential can be sufficiently described with nonrelativistic pseudopotentials

[Animalu 1966]. Within about 0.1 nm these potentials are square wells whose depth is dependent on angular momentum. Outside this distance the potential becomes coulombic, with the charge determined by the atomic valence. Atoms of the same valence will then form a square well with a width of about 0.1nm, which is less than the nearest neighbor distance. Therefore in an isoelectronic system which forms an electron trap, (i.e., ZnS:O) the description of the impurity potential simplifies to a localized potential with a depth corresponding to the difference between the s state pseudopotentials of the host atom and the impurity atom. In an isoelectronic series of atoms, the pseudopotential depth for s states are in general, higher for the lighter atoms in the sequence [Animalu 1966]. It follows then that if a host atom is replaced with a lighter atom from its series, the impurity potential will attract electrons. In general the electronegativity of a series decreases as the atomic weight goes up. These observations summarize the electronegativity rule; when the isoelectronic impurity is more electronegative and lighter (lower atomic weight) than the host atom the resulting impurity potential will attract electrons.

These differences also cause isoelectronic substitution atoms to have a limited solubility in the host matrix. Even though the valence structure is the same, the atomic (size ect.) differences are sufficient to form a carrier trap. This also causes the substitution to be energetically unfavorable and limits the number of impurities in a given volume of host material. Which means that the number of traps should be expected to reach some maximum value. Under constant power conditions, the proportion of total electrons trapped should approach a constant value at saturation

and the concentration of carriers available for other processes in the material would stabilize.

Effects of Oxygen in Zinc Sulfide

The effects of oxygen addition on ZnS have been investigated in both the ZnS:Cu and the ZnS:Au systems. Samples prepared with additional ZnO show a much stronger and longer phosphorescence (or afterglow, referring to luminescence produced after excitation has stopped which is caused by the release of carriers from traps) than those prepared without oxygen present [Kroeger and Dikhoff 1952]. Oxygen free samples have a single glow peak with a maximum at -80^0 C, whereas samples prepared with the addition of 1 mole % ZnO show three peaks at -100^0, -25^0 to -50^0, and $+52^0$ C. The peak above room temperature is responsible for the strong room temperature phosphorescence. The identical nature of the high temperature glow peaks found in both ZnS:Au and ZnS:Cu strongly suggests that the traps responsible cannot be characteristic of copper or gold alone [Garlick et al. 1949]. It is possible, of course, that Cu and Au caused exactly identical traps, but this is not very probable considering that the centers of luminescence formed by these ions are not identical. It is therefore reasonable to assume that the traps were formed by oxygen
[Kroeger and Dikhoff 1952]. Similar peaks were not formed in the ZnS:O,Ag system which can be explained on the basis of hole migration [Schon 1954, Klasens 1958, Kroeger 1948]. According to this theory, holes trapped in centers within the bandgap will be re-emitted into the valence band above the critical temperature determined by

the depth of the trap relative to the band edge. This free hole may migrate to lattice defects and recombine with an electron from the conduction band or one already localized on the trap [Nail et al. 1949, Roberts and Williams 1950]. For Cu and Au the gap between the luminescent level and the band edge is so large (~1.0 eV) that electrons are first thermalized (re-emitted from the trap by thermal energy) out of the oxygen traps. These free electrons subsequently migrate to the luminescent center and recombine radiatively with the trapped holes. For Ag however, the trap level is much closer (~0.3 eV) to the band edge and all the holes are re-emitted into the valence band before electrons can move out of the oxygen traps and almost no phosphorescence is observed.

The effects of oxygen can not be attributed to the formation of a ZnS-ZnO solid solution. The addition of a small amount of ZnO in ZnS would cause a slight contraction of the ZnS lattice, similar to the effect of cooling or compressing the sample [Seiwert 1949]. Reduced bond lengths should result in a shift of the absorption edge toward shorter wavelengths, whereas the opposite has been observed experimentally [Kroeger and Dikhoff 1952]. These authors also commented that the magnitude of the shift was much larger than what would be expected from the small variation of unit cell dimension actually observed. The effects must therefore be due to the effects of the oxygen in the ZnS lattice, specifically the formation of an isoelectronic trap.
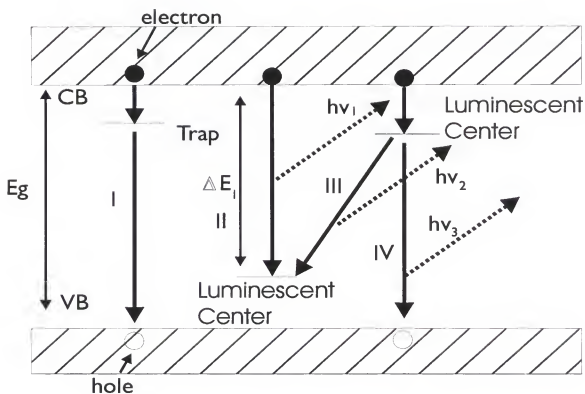
Figure 2.1. Schematic of a nonradiative relaxation (I) and three possible
radiative transitions (II-IV) for excited electrons in a luminescent
solid. The energy of the emitted photon (hv) is determined by the energy
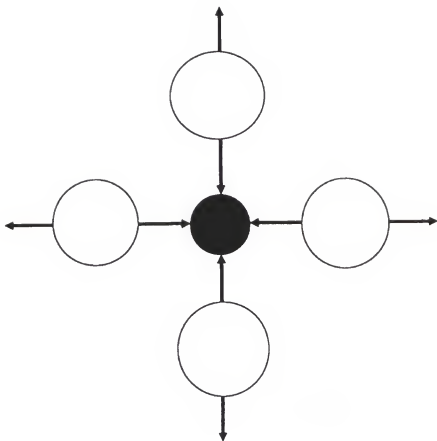difference between the two levels utilized in the radiative transition.

Figure 2.2.   Symmetric stretching vibration of a square planar complex. The ligands
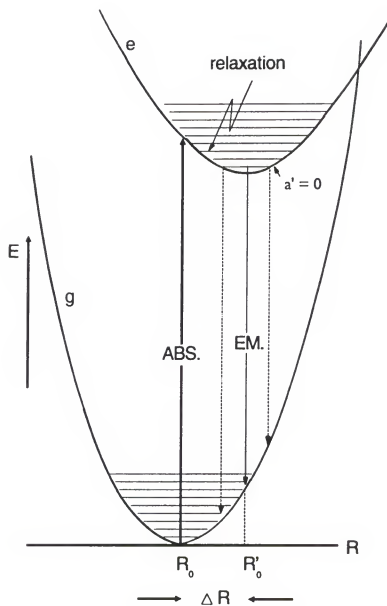   (open circles) move in phase toward and away from the central metal ion,
                as shown by the arrows.

Figure 2.3. Configurational coordinate diagram. Absorption has been drawn as a single line for clarity [Blasse and Grabmaier 1994].
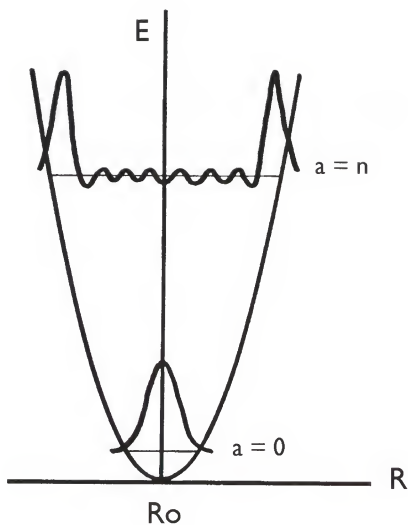
Figure 2.4.   Vibrational wave functions for the lowest vibrational level (a=0) and a high vibrational level (a=n) [Blasse and Grabmaier 1994].
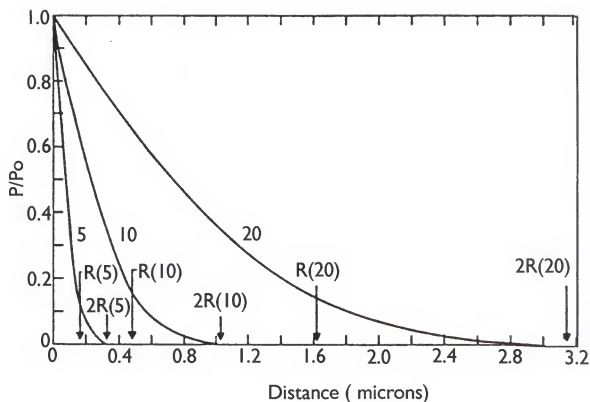
Figure 2.5. Relative power per unit area of an electon beam traversing ZnS. Arrows indicate the range (R) for 5, 10, or 20 keV from Markov's expression (equation 2.12)) and twice the range (2R) for 5, 10, and 20 keV electrons [Kingsley and Prener 1972].
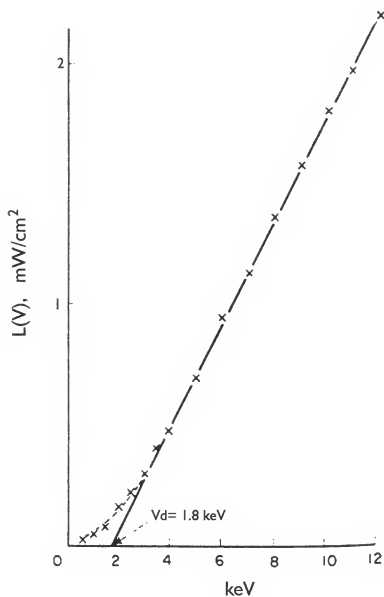
Figure 2.6.   Cathodoluminescent brightness vs. voltage curve for ZnS:Ag,Cl
[Gergely 1960].
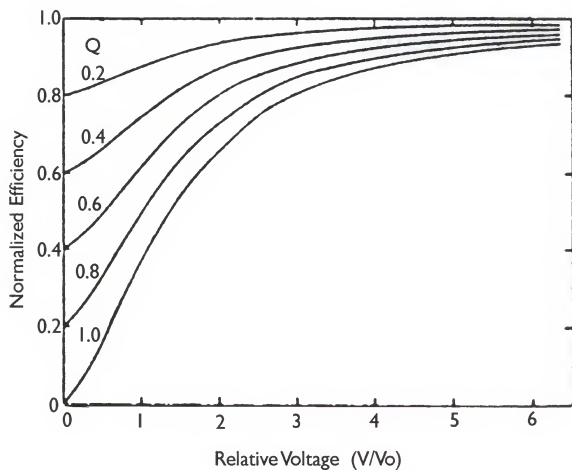
Figure 2.7. Theoretical curves for normalized cathode-ray efficiency as a function of voltage for different strengths of surface recombination (Q) [Ludwig and Kingsley 1970].
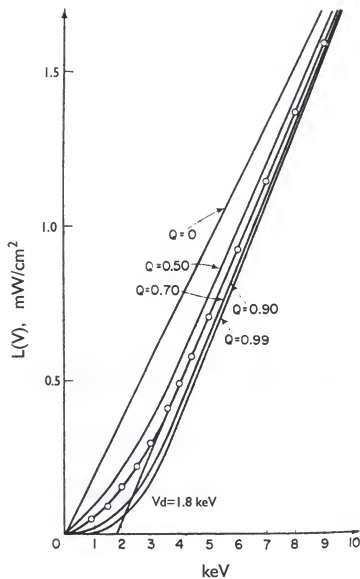
Figure 2.8.   Theoretical brightness vs. primary beam energy curves for various Q (cm²-sec) values. Experimental points denoted by circles (O) [Gergely 1960].
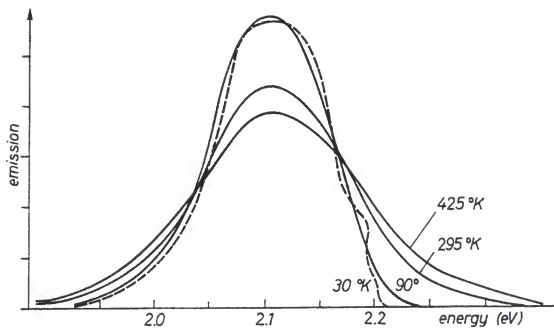
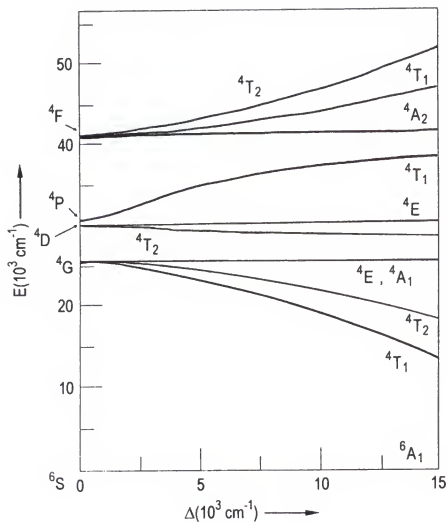Figure 2.9.   ZnS:Mn emission spectra in arbitrary units as a function of temperature [Balkanski et al. 1966].

Figure 2.10.   Tanabe-Sugano diagram for the d^5 configuration as a function of the
                octahedral crystal field. Free ion levels are on the left side, crystal field
                levels on the right. Doublets have been omitted for clarity
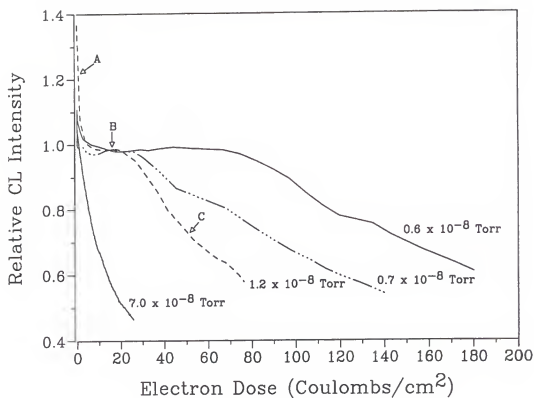   [Blasse and Grabmaier 1994].

Figure 2.11.   Relative CL intensity versus electron dose at 2 keV in several different background pressures as indicated [Swart et al. 1997].
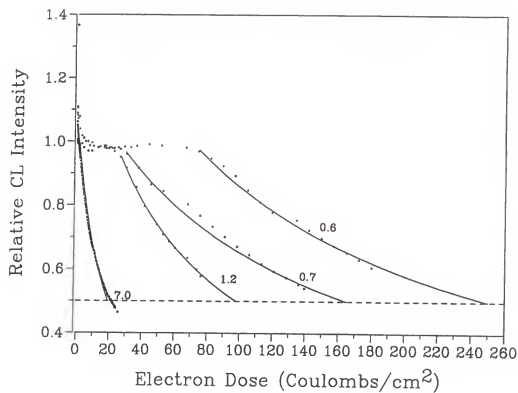
Figure 2.12. Relative CL intensity versus electron dose at 2 keV in several different
background pressures (x10⁻⁸ Torr) and the best fitted curves for region C
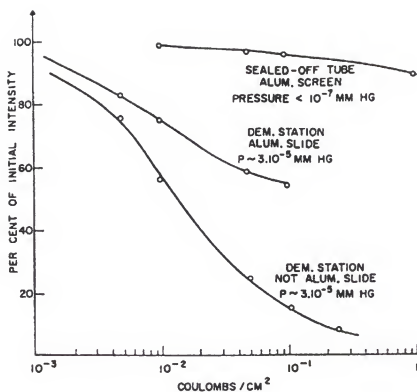[Swart et al. 1997].

Figure 2.13. Effects of vacuum ambient and aluminazation on the performance of a ZnO phosphor [Pfhahnl 1961].
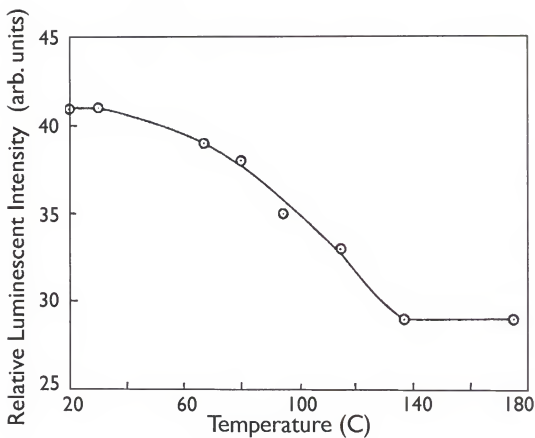
Figure 2.14.   Isochronal annealing characteristics of a zinc sulfide powder previously irradiated at 77° K with electrons of 190 keV energy [Bryant and Manning 1972].
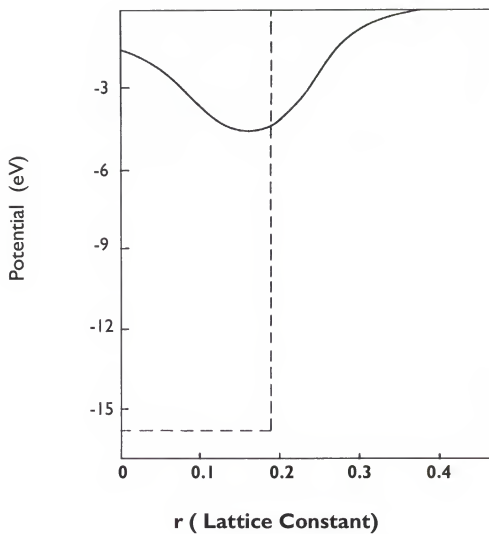
Figure 2.15. Nonrelativistic impurity potential for the system GaP:Sb. The broken line is the unscreened impurity potential in the no-relaxation case. The solid line includes both screening and relaxation [Baldereschi 1973].

CHAPTER 3
EXPERIMENTAL

Sample Preparation

Samples of ZnS:Mn thin films were deposited by metalorganic chemical vapor deposition (MOCVD) on silicon (100) wafers at the University of Florida [Yu 1994]. An rf heated modified Spire model SPI-MOCVD 450 horizontal tubular reactor was used for film growth. The precursors for ZnS growth were diethylzinc from Air Products Chemicals Inc. of 99.9998% purity, and hydrogen sulfide from Solkalronic Chemicals of 99.99% purity. An undoped layer was first deposited on the silicon at 350^0C, followed by the Mn doped layer deposited at 475^0C. The Mn doped layer was deposited using tricarbonylmethylcyclopentadienyl-Mn (TCMn) of at least 99.999% purity. Table 3.1 gives a summary of the typical growth conditions for both the ZnS and ZnS:Mn layers. Post deposition SIMS analysis showed the Mn concentration in the second layer to be approximately 0.5 mol %.

The ZnS single crystal samples grown by high temperature evaporation were obtained from Eagle-Picher. They were sent to Spire Corporation and ion implanted with Mn at 185 keV, to a dose of 5×10^{15} Mn/cm^2. Following implantation, the samples were annealed in 10% H$_2$S, 90% argon at 800^0C for one hour to recrystalize the surface and activate the implanted Mn. The single crystals were analyzed with high resolution

49

x-ray diffraction (HRXRD), discussed later, as received, after implantation and after anneal to determine the crystal quality at each step.

Auger Electron Spectroscopy (AES)

Because much of the focus of this research is on the surface reactions that occur during ageing of ZnS phosphors, Auger electron spectroscopy (AES) [Holloway 1980] was chosen as the primary characterization technique because of its surface sensitivity. This is significant because the reactions under investigation were expected to affect only the first few atomic layers of the material. The emission of Auger electrons results from the radiationless rearrangement of electrons in an excited atom. During AES, the sample is normally excited with a primary electron beam which removes core electrons from the atoms in the solid. For the atom to return to the ground state, outer orbital electrons fill the missing core electron orbitals. The energy difference between the outer and core levels is transferred to, and causes the emission of, Auger electrons (Figure 3.1). These electrons have low energy (typically 20-2000 eV) and consequently have a very limited escape depth from the sample. Auger information is therefore typically collected from only the first 1-5 nm of the material [Holloway 1980].

In situ AES (PHI model 545 spectrometer) was used to monitor the surface composition of the ZnS:Mn during electron bombardment. The Auger spectrometer system was mounted in a UHV vacuum chamber which was rough pumped by oil-less cryogenic sorption pumps, then ion (Perkin-Elmer Ultek D1) pumped to ultra-high vacuum (UHV). The films were bombarded with a primary electron beam (1 to 4 keV,

1.5 to 15μA, 300 um to 1100 um beam diameter, 1.1x10^{-3} A/cm^2 typical current density)
over a range of pressures from 1x10^{-6} to 5x10^{-9} Torr, with a system base pressure of
1x10^{-9} Torr. Auger spectra were taken from 30 to 1000 eV for all primary beam
energies (E$_p$) above 1 keV. At 1 keV spectra were recorded from 30 to 550 eV. Auger
data were collected with a single pass CMA and lock in amplifier in the derivative mode,
using a peak to peak modulation of 4 eV. Spectra were collected continuously by an
analog to digital converter, and a typical spectra would be collected in between 1 to 5
minutes, depending on the energy scan rate. Changes in surface composition were
monitored by following changes in the Auger peak to peak heights (APPH) of the
elements present.

For samples that were sputtered, an argon ion beam of 3 keV from an emission
current of 10 mA was rastered over a 10mm x 10mm area. For an argon pressure of
2x10^{-5} Torr, the sputter rate was approximately 0.25 nm/min, as determined by
sputtering through a 40 nm thick ZnO film.

The samples were mounted on a carousel such that the surface normal was 30^0
from the Auger CMA axis (Figure 3.2). All samples were mounted with metal clips
directly to the stainless surface of the sample holder to provide maximum conductivity.

Control of the Vacuum Ambient

In order to assess the effects of the vacuum ambient on the degradation of ZnS
phosphors, hydrogen, oxygen, and argon of 99.999% purity and hydrogen sulfide of
99.98% purity were back-filled into the UHV chamber to pressures ranging from 5x10^{-8}

to 1×10^{-6} Torr, as measured by an ionization gauge. For testing water vapor, the ion vacuum pump was throttled to a low pumping speed and the residual vacuum background gas pressures were allowed to rise. Spectra from a UTI 100C quadrupole mass analyzer (Figure 3.3) showed the "residual gas" ambient to be predominantly water vapor, with small amounts of methane, CO, CO_2, H_2 and H.

Analysis of Luminescence

A quartz view port located approximately 60^0 relative to the incident electron beam, allowed simultaneous collection of cathodoluminescent data during electron bombardment (Figure 3.3). The light emitted from the ZnS samples was focused onto the entrance slit (50 um) of a 77400 Oriel MultiSpec spectrometer using a 600 line/inch diffraction grating, with an InstaSpec charge coupled device (CCD) detector, for spectral analysis and relative brightness comparisons. Spectra were periodically gathered between 450 and 650 nm during the course of the experiments, and data were plotted as relative peak intensity brightness vs. wavelength.

High Resolution X-Ray Diffraction (HRXRD)

A Philips HR1 x-ray diffractometer (Figure 3.4) was used to perform x-ray analysis on the single crystal ZnS samples to ensure that the original quality of the crystal was recovered during the post implant anneal. The x-ray generator was run at 40kV and 40 mA which produced Cu Ka radiation at a wavelength (λ) of 0.154056 nm.

The radiation was conditioned by a 4-crystal monochromator (Figure 3.5) to produce radiation with a 12 arcsec divergence, a wavelength spread of $\Delta\lambda/\lambda = 2.3 \times 10^{-5}$, and a beam approximately 5mm in diameter. In addition the radiation was diffracted by a crystal between the sample and the detector. The analyzer crystal is a U-shaped (Bonse-Hart) crystal which was mounted directly in front of the detector to increase the resolution. The geometry of the crystal with respect to the monochomator, sample, and detector is shown in figure 3.5. The improved resolution was a direct result of limiting the acceptance angle to 14 arcsec, which allows the separation of lattice parameter and misorientation contributions to diffraction peak broadening. X-ray analysis performed with a 4-crystal monochromator is generally referred to as high-resolution x-ray diffraction (HRXRD) [Bartels 1983, He and Razeghi 1993, Heinke et al. 1994].

The goniometer and diffractometer arrangement are shown in figure 3.4. The single crystal samples were mounted on the goniometer with tape on the mounting plate. The sample surface was aligned to the center of the optical axis with a dial gauge which was inserted at the base of the goniometer. To optimize the signal to noise ratio, a series of rocking curves were recorded and both rotation and tilt were adjusted until the maximum diffracted intensity and smallest line width was achieved. The data were recorded as x-ray maps of omega vs. omega/2 theta, and the x-ray intensity is represented by concentric isointensity rings in this two dimensional space. In general broadening in the omega direction is caused by mistilt among crystallites, often referred to as mosaic structure, and broadening in the omega/2 theta direction indicates

deviations in lattice parameter which are most commonly caused by stress in the material [Alexander 1995].

Secondary Ion Mass Spectrometry (SIMS)

Secondary ion mass spectrometry or SIMS [Benninghoven et al. 1987, Brundle et al. 1992] was used to characterize the elemental composition of the near surface region of the ZnS samples. SIMS operates by bombarding the surface of the sample with heavy (O_2 or Cs) ions or neutrals. During bombardment, surface particles are sputtered from the surface of the sample, and they can be positively or negatively charged, neutral, or excited atoms and molecules. Secondary ion emission includes all the emitted surface particles in both the ground and excited states [Benninghoven et al. 1987]. Virtually all these secondary ions are generated in the uppermost atomic layers of the sample surface, and are easily separated by several types of mass analyzers.

SIMS raw depth profiles and mass surveys of the single crystal ZnS samples were obtained with a Perkin-Elmer 6600 SIMS system. A 5 keV Cs^+ primary ion beam and negative ion detection were used. The primary ion beam current was set at 60 nA, the acceleration voltage was 100 V, and the raster size was 350×350 um^2 with a 75% gating. The resulting detected area was 87.5×87.5 um^2. Hydrogen, carbon, oxygen, sulfur, and ZnS were monitored using masses $^1H^-$, $^{12}C^-$, $^{16}O^-$, $^{34}S^-$, and $^{100}ZnS^-$, respectively. These analysis conditions were chosen to maximize the sensitivity for and depth resolution of the oxygen in this sample. The raw data have been processed into

atom ratio vs. depth. The signals of the species of interest have also been normalized to the constant matrix signal of sulfur to account for intensity changes due to analysis and matrix effects, this allows for more accurate comparison between different samples.

<u>X-Ray Photoelectron Spectroscopy (XPS)</u>

X-Ray photoelectron spectroscopy (XPS) is quite similar to AES, absorption of an X-ray photon ejects a core electron from a surface atom and causes the emission of a photoelectron by relaxation [Brundle et al. 1992] Due to their energy, these photoelectrons can travel only short distances in the sample before losing energy from atomic collisions, which gives XPS surface sensitivity as good as AES. However, the main advantage of XPS is its sensitive chemical state analysis, which shows shifts in XPS peaks based on the local surroundings (bonding) of the atoms. These shifts allow the experienced XPS operator to differentiate between Zn atoms bonded to oxygen and those bonded to sulfur on the surface of the phosphor.

XPS was performed on a ZnS sample before and after degradation at 1×10^{-6} Torr oxygen pressure, with a 2keV electron beam to a terminal dose of 4500C/cm^2. The electron beam was 110 um in diameter, with a continuous current density of 52 mA/cm^2. The XPS system was a PHI Model 549 system, equipped with a double pass CMA. The Mg X-ray source was operated at 300W (15kV) yielding a photon energy of 1253.6 eV. A pass energy of 25 eV was used.

<u>Activator Efficiency Measurements</u>

One way to monitor changes in a luminescent activator is to compare changes in the decay of luminescence from the excited state between two samples, in this case between as-deposited and degraded samples. This was accomplished by exciting the sample with an electron pulse, and recording the decay of the luminescent intensity with time. The decay curves obtained by this method can be used for direct comparison of activator efficiency, i.e., a curve that shows lower brightness during decay indicates a lower activator efficiency in that sample. A Reflection High Energy Electron Diffraction system (RHEED) from Staib Instrumente (model # EK-2035-S) was used to measure the luminescent transients at the University of Georgia. To pulse the gun, a Fast Beam Pulser (EK-35PB) was used, which was also purchased from Staib Instrumente. A range of beam energies from 500 eV to 35 keV were available, and both 2 keV and 9 keV were used for the thin film samples. Beam currents ranged from 100 nA to 300 microamps, depending on the acceleration voltage of the gun. The gun was externally pulsed with a Stanford Pulse Generator DG535 for a 1 microsecond pulse width with a 10 ms repetition period. During pulsing the beam current was measured using a Faraday cup was approximately 1.4 nA. A H-10 monochromator (Jobin-Yvon) filtered the luminescent signal before it entered an Oriel 77341 photomultiplier tube (PMT) operated at 1200 V for signal detection. The Oriel tube has a rise time of 2.2 ns and a spectral range of 185 nm to 870 nm. An EG&G Turbo MCS (multichannel scalar) interface was used for data acquisition.

During excitation of as deposited samples, a 0.3 neutral density filter was used to avoid saturation of the PMT/MCS. However because of the lower luminescent output of the degraded samples, no filter was necessary. In order to achieve a reasonable signal to noise ratio, the electron beam was deflected approximately 15^0 off normal by means of low aberration magnetic coils. This geometry was chosen so that the light from the RHEED filament was not reflected off the sample holder and into the PMT.

Thermoluminescent (Glow) Experiments

Although the term thermoluminescence is commonly used to describe the light emitted from a material when heated above room temperature, it is also appropriate to describe a phosphor that has been excited while cold and emits light during warming [Randall and Wilkins 1945]. The thermoluminescent light emission curve is often referred to as a glow curve. A glow experiment yields a plot of light emission vs. temperature as the phosphor is warmed at a uniform rate. It is generally assumed [Johnson 1939] that the glow is due to the release of electrons from traps in the material. These re-emitted electrons migrate to luminescent centers and produce the observed light.

Thermoluminescence was performed on both degraded and reference single crystal ZnS:Mn samples at a base pressure of 1×10^{-7} Torr. The degraded sample was bombarded at 2 keV in 1×10^{-6} Torr oxygen to form approximately 3 nm of oxide on the surface. Both samples were mounted on a liquid nitrogen cooled cold finger and a thermocouple was attached to the surface of the samples. The samples were cooled to

liquid nitrogen temperatures and bombarded with 2 keV electrons from a Kimball Physics EFG-7 electron gun to fill the traps in the material. At this point the electron gun was switched off and a small heater at the end of the cold finger was used to maintain a constant 2-3 ^{0}C/min. warming rate, from -196^{0}C to 0^{0}C. The light output from the samples was monitored with an Ocean Optics spectrometer and fiberoptic light collection focused on the sample surface.

Table 3.1. Summary of typical growth conditions for ZnS and ZnS:Mn [Yu 1994].

	Undoped ZnS	ZnS:Mn
Substrate Temperature:	350-400^{0}C	450-550^{0}C
Growth Time:	15 min.	15min.
Reactor Pressure:	50 Torr	
Total Hydrogen Flow Rate:	4.0 slm	
DEZn Mole Fraction:	1.0×10^{-4}	
H$_2$S Mole Fraction:	100.0×10^{-4}	
VI/II Inlet Ratio:	100	
TCMn Mole Fraction:	1.5×10^{-6} to 7.5×10^{-6}	
TCMn Bubbler Temperature:	30^{0}C	
Pressure:	200 Torr	
H$_2$ Flow Rate:	10 to 50 sccm	
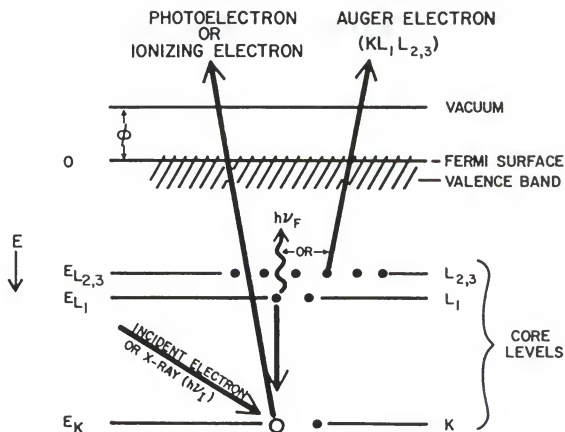
Figure 3.1.   Energy level diagram of the electronic states in a solid and a schematic illustration of the Auger process [Holloway 1980].
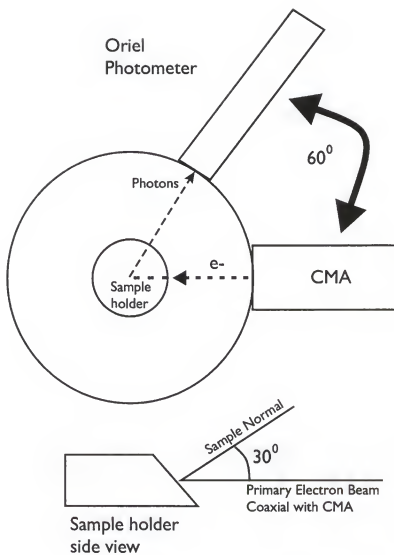
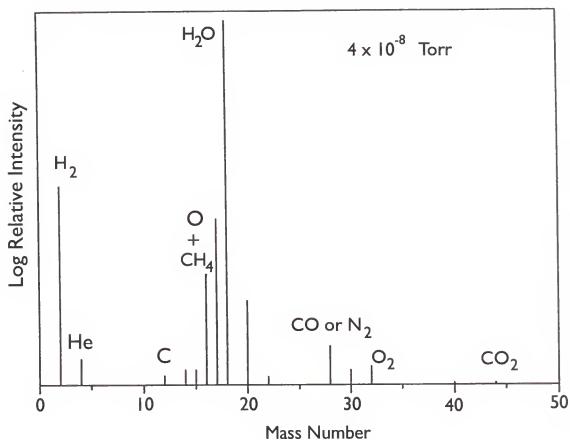Figure 3.2. Schematic of Auger and cathodoluminescence vacuum chamber geometry.

Figure 3.3. Residual gas analysis of typical vacuum ambient during "water vapor" Auger experiments.
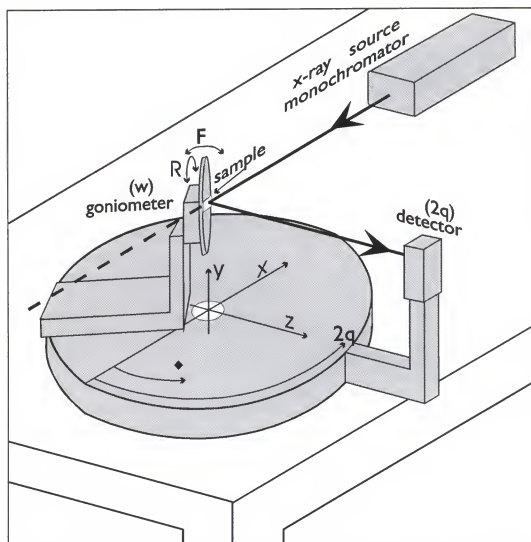
Figure 3.4.   View of the goinometer and diffractometer arrangement used for HRXRD [Alexander 1995].
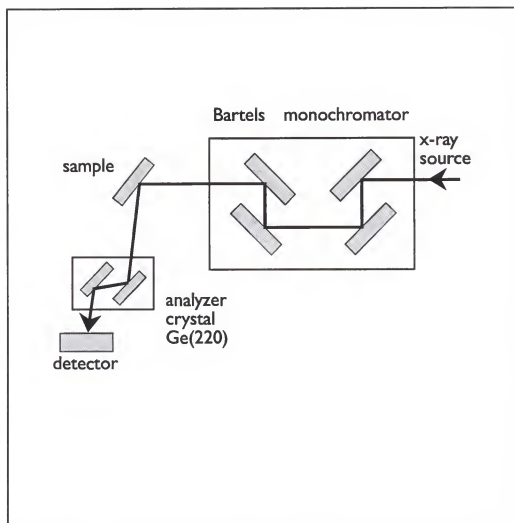
Figure 3.5.   Geometry of the analyser crystal with respect to the monochromator, sample and detector [Alexander 1995].

CHAPTER 4
RESULTS

Auger Electron Spectroscopy (AES) of ZnS Thin Films

Changes in the surface chemistry of the samples were monitored with AES. Figure 4.1 shows typical AES spectra from before and after a ZnS:Mn sample was bombarded by a 2 keV electron beam (750 um diameter) in 1×10^{-7} Torr oxygen to a charge load of 200 C/cm^2 (1.1 mA/cm^2 for 50 hours). Sulfur and oxygen were monitored by using the 152 ev and 510 ev Auger peaks, respectively [Davis et al. 1976]. Zinc can be monitored by either its 59 eV or 994 eV peak and typically both were recorded. Carbon which was present from handling and hydrocarbon contamination was monitored by its peak at 272 eV. Note the virtual disappearance of the sulfur Auger peak and the large increase in the oxygen peak. Similar changes with different rate constants were observed in samples bombarded in hydrogen and water vapor. However, no such changes in Auger signal intensities were observed for samples bombarded in an argon ambient, or for samples exposed to oxygen without electron bombardment. In addition, samples bombarded at vacuum levels of 10^{-9} Torr or better, showed little (<1%) or no change in surface chemistry.

Figure 4.2 shows typical results from AES analysis during phosphor degradation. The Auger peak-to-peak heights (APPH) in arbitrary units for zinc, sulfur, oxygen, and

carbon are plotted versus the coulombic dose (C/cm^2 where C = amp-sec). These data were collected for 4 keV electrons at 5×10^{-8} Torr in water vapor. During bombardment, both the sulfur and carbon signals decreased steadily, while the zinc and oxygen signals increased and appear to saturate at about 200 C/cm^2. The amount of carbon present on the surface of the phosphor decreased exponentially with increased electron dose, until the signal was lost in the noise at about 100 C/cm^2. Concurrent with the decrease of the carbon signal from 0 to 100 C/cm^2, both the low (59 eV) and high (994 eV) energy zinc signals increased. APPH vs. electron dose with the primary beam energy reduced from 4 keV to 1 keV in 5×10^{-8} Torr water vapor are shown in figure 4.3. Under these conditions, the 994 eV Zn peak can not be excited by the 1 keV primary beam and consequently it is not plotted . The behavior of the elements are similar to the previous experiment, where the oxygen and zinc signals increase and the sulfur and carbon signals decrease over the course of the experiment. The zinc signal does not, however, increase from the beginning of the experiment as it does in the 4 keV plot (Figure 4.2) but remains fairly constant until a dose of 5 C/cm^2 and begins to increase from this electron dose. Also note that the carbon is reduced to 10% of its initial value at 12 C/cm^2, while the same reduction required 100 C/cm^2 at 4 keV. Figure 4.4 is a similar plot of Auger signal intensities taken during 2 keV electron bombardment in 5×10^{-8} Torr in water vapor. The behavior of the Zn, C, and O peaks are similar to the 4 keV plot, however the sulfur signal remains fairly constant up to about 30 C/cm^2, and then increases approximately 10% before it begins to decrease at 60 C/cm^2. Note that this is the same electron dose where the carbon signal has decreased to a low (near zero) level.

A series of degradation experiments were also performed at 1 keV and 1×10^{-6} Torr of four different vacuum ambients. Figure 4.5 shows the first of these experiments run in hydrogen. The zinc and oxygen signals increase only slightly during the experiment, while the sulfur and carbon signals decrease more or less linearly. Similar data collected from an oxygen ambient are shown in figure 4.6, and the zinc signal nearly doubles as the oxygen signal increases to ten times its original value during the course of the experiment. The sulfur signal also shows significant change in signal intensity decreasing from 170 (arbitrary units) at the beginning of the experiment to 20 by 15 C/cm^2. The third experiment of this series was performed in a 1:1 mixture of oxygen and hydrogen. Figure 4.7 shows that the zinc signal increases slowly as does the oxygen signal from an initial relative value of 1.5 to 3.5 at the end of bombardment. This is a much smaller increase than was observed during the oxygen experiment, however the decrease of the sulfur signal is more rapid reaching 15 % is its initial value by 10 C/cm^2. This same amount of decreased sulfur signal was achieved in 13 C/cm^2 during the oxygen experiment. The results of the final experiment performed in water vapor are shown in figure 4.8. Both the zinc and oxygen signals increase rapidly up to 4 C/cm^2 where they both appear to saturate and the signals remain constant for the remainder of the experiment. The carbon signal decreases rapidly to the same point (4 C/cm^2) where its signal is lost in the noise level of the experiment. The sulfur signal also decreases rapidly reaching 15% of its original value at 8 C/cm^2. Having demonstrated that electron bombardment in various vacuum ambient cause chemical changes on the surface of the phosphor, what remained was to relate the surface chemical changes to changes in the luminescent characteristics of the phosphor.

Concurrent Auger and Cathodoluminescence

To investigate the correlation between the surface chemical changes and the cathodoluminescent brightness of the phosphor films, the Oriel spectrometer was aligned on the AES vacuum system as discussed in chapter 3 to allow simultaneous collection of CL and AES data. Figure 4.9 shows typical concurrent AES and CL results collected at 2 keV in 5×10^{-8} Torr of oxygen. The brightness of the phosphor film was stable as long as the carbon contamination was present, and even increased slightly (~5%) as the carbon signal dropped. A similar increase was also apparent in the sulfur signal which climbs 15% during the decrease of the carbon signal. However, once the carbon signal decreased to near zero at a dose of 40 C/cm^2, the sulfur signal began to decrease followed shortly thereafter by a decrease in the cathodoluminescent brightness. Luminescent spectra plotted as cathodoluminescent intensity vs. wavelength (Figure 4.10), collected periodically during degradation showed no change in either the peak wavelength or the shape of the luminescent spectra during degradation.

Figure 4.11 shows a second plot of concurrent AES and CL for an experiment at 4 keV in 1×10^{-6} Torr oxygen. Both the carbon and sulfur signals decreased from the beginning of the experiment and were lost in the experimental noise level by 100 and 280 C/cm^2, respectively. The zinc signal increased and appeared to saturate at approximately twice its original intensity after 100 C/cm^2. The oxygen signal also increases from the beginning of degradation, and saturates at 200 C/cm^2. The relative CL intensity declined slowly between 0 to 70 C/cm^2, after which it began to decline more rapidly reaching 57% of original intensity by 150 C/cm^2. From this coulombic load until the end of the

experiment the decline of CL intensity is linear. It is interesting to note however, that the CL intensity continued to decline after both the oxygen and sulfur signals were no longer exhibiting any change in intensity. Auger and CL data collected at 2 and 1 keV are shown in figures 4.12 and 4.13 respectively, and both of these plots demonstrate behavior similar to that shown in figure 4.11. The most significant difference among these three plots is the reduced coulombic loading necessary to produce similar changes in both the Auger and CL signal intensities, as the primary beam voltage is reduced. The 4 keV plot reaches 50% relative CL brightness in 220 C/cm^2, while the 2 keV and 1 keV plots require only 120 and 12 C/cm^2 respectively.

Auger and cathodoluminescent data collected in H_2S at 1×10^{-6} Torr are shown in figure 4.14. The zinc and oxygen signals decreased 20% from 0 to 40 C/cm^2 and remained steady for the remainder of the experiment. The sulfur signal climbed from the beginning to 50 C/cm^2 and then appeared to saturate and remains constant at twice its original APPH. The relative CL intensity climbed from 95% to 100% by 50 C/cm^2 and then decreased slowly until 200 C/cm^2 where it has reached 92%. Immediately following this experiment in H_2S, the same sample was degraded at 2 keV in oxygen at 1×10^{-6} Torr and the results were plotted in figure 4.15. The oxygen signal increased linearly throughout the experiment, however there is a change in slope at 100 C/cm^2 and the rate increased. The zinc signal remained constant until 150 C/cm^2 and then increased linearly until the end of the experiment. Both the sulfur and CL signals were stable until 100 and 120 C/cm^2 respectively at which point they both decreased until 200 C/cm^2.

Figure 4.16 also shows concurrent cathodoluminescent and APPH data for a sample which was bombarded in H_2S at 2 keV. The sample was then degraded in oxygen at 2 keV, and finally bombarded in H_2S at 2 keV and 1 keV. The pressure throughout the experiment was 1×10^{-6} Torr. The carbon signal decreased rapidly and is lost by 200 C/cm^2. The zinc signal increased from 0.18 to 0.20 during the first H_2S bombardment, decreased to approximately its original value during bombardment in oxygen, and remained fairly constant for the remainder of the experiment. The oxygen signal decreased from 0.25 to 0.21 during the first H_2S bombardment, then increased to 0.45 during degradation in oxygen, and finally decreased again during bombardment in H_2S to 0.10 by 350 C/cm^2. Sulfur increased from 0.65 to 0.75 during the first H_2S bombardment and remained at this value for 40 C/cm^2 after degradation in oxygen had begun. Its signal then dropped to 0.08 by 200 C/cm^2, however as soon as bombardment in H_2S was resumed the sulfur signal increased to 1.0 by 300 C/cm^2 and saturated at this value. The relative CL intensity followed a similar pattern, remaining steady at 0.95 until 100 C/cm^2 and declining during degradation in oxygen to 0.48. The CL intensity then remained at this value during bombardment in H_2S at 2 keV and increased only after the primary beam voltage was decreased to 1 keV at 550 C/cm^2. By 750 C/cm^2 the CL intensity had reached 0.90 and remained at this value until the end of the experiment. It is important to note that the data contained in figure 4.16 are a composite of 10 sequential experiments. For ease of viewing and interpretation, the data were normalized to account for differences between the signal levels at the end of one experiment and the beginning of the next. This is especially significant when the beam voltage was reduced from 2 keV to 1 keV. In this case both the Auger and CL signals

had significantly lower absolute values. To assure accurate comparison of the data at different primary beam voltages, the beam voltage was periodically increased to 2 keV during the recovery of CL brightness at 1 keV to verify that the absolute value of brightness was comparable to the values obtained during the beginning of the experiment.

Sputter Experiments on ZnS Thin Film and Single Crystal Samples

Early in our experimental program, the surface was sputter cleaned prior to running a degradation experiment to remove any surface contamination from the phosphor. Sputter cleaning is frequently performed on Auger samples exposed to atmosphere prior to analysis to remove any contaminates from the atmosphere or handling. This procedure did not appear to influence the Auger chemical information collected from the samples, other than eliminate adventitious carbon contamination from the surface.

Effects of Sputtering on Cathodoluminescent Intensity

Sputtering did however have a dramatic impact on the cathodoluminescent brightness of the samples. Figure 4.17 shows the relative cathodoluminescent brightness of a ZnS:Mn thin film phosphor vs. the sputter time in minutes for 3 keV Ar^+. There is a large initial drop in brightness during the first few minutes of sputtering, followed by nearly exponential brightness loss as sputtering continues. After 150

minutes of sputtering the brightness had decreased to about 15% of the original intensity.

A complimentary sputter experiment was performed on a ZnS single crystal sample and the relative brightness vs. sputter time plot is shown in figure 4.18. This sample demonstrates a similar loss of brightness during sputter as compared to the thin film sample. However this sample was characterized with high resolution x-ray diffraction both before and after sputter and these results are detailed in a later section. Once this effect of sputter on CL brightness was confirmed, further degradation experiments were begun without the initial sputter cleaning. Sputter profiling was used only to gather post degradation information on the phosphor surface oxides.

Analysis of ZnO Surface Layer Thickness

To determine the thickness of the oxide layers on the surface of the ZnS samples after degradation, the surface region was sputter depth profiled by AES. By sputtering at a known rate (0.25nm/min, see chapter 3) the thickness of the oxide layers could be determined. The interface between the ZnO layer and underlying ZnS was defined as the time required to reduce the oxygen signal to 50% of its original intensity (Figure 4.19). By using this method the thickness of the ZnO layer was determined to be approximately 3 nm for a sample degraded by 2 keV primary electrons in oxygen at 1×10^{-6} Torr to a dose of 120 C/cm^2.

Optical Absorption in ZnO Surface Layer

The formation of a non-luminescent ZnO layer over the ZnS phosphor could change the brightness of CL from the sample by absorbing light or attenuating the primary electron beam. To account for these possibilities, the ZnO layer was removed by sputtering to determine if the original brightness could be recovered. Figure 4.20 shows a plot of sputter time vs. cathodoluminescent brightness for a degraded ZnS:Mn phosphor. The sample had previously been degraded in an oxygen ambient at 1×10^{-6} Torr with 2 keV primary electrons to form approximately 3 nm of ZnO on the surface, which resulted in a reduction of the light output to 53% of its original value. The ZnO layer was sputtered at 0.25 nm/min and the interface between the ZnO and ZnS is indicated with a dashed line at 12 minutes. The cathodoluminescent brightness of the phosphor climbs about 8% over its initial value after 12 minutes of sputtering, and then declines rapidly as the ZnS is sputtered, similar to the ZnS sputter experiment described above. It is also interesting to note that during the hydrogen sulfide experiment in figure 4.16 there was no increase in CL brightness during the decrease in oxygen signal while the sample was being bombarded in hydrogen sulfide after degradation in oxygen.

Possible brightness changes due to optical absorption in the oxide layer were further evaluated by using a 414 nm thick (determined by atomic force microscopy) ZnO film RF sputter deposited from an intrinsic ZnO target on a 2 mm thick silica substrate obtained from Battelle. This sample showed 62% absorption at 550 nm, which corresponds to a damping (k) constant of 0.102 (see Appendix A). At the typical oxide thickness for a degraded sample (3 nm) this damping constant corresponds to 0.7%

absorption of the light produced in the underlying phosphor. This seems to be a reasonable number considering that the oxide layer is not generally visible during reflection optical microscopy of a degraded sample. In addition, 125 nm of ZnO was deposited by RF magnetron sputtering on a portion of a ZnS:Mn thin film sample. CL brightness measurements at 2 keV showed a 16% lower CL brightness in the coated as compared to the uncoated areas. The significance of these results will be discussed in chapter 5.

<u>High Resolution X-Ray Diffraction (HRXRD)</u>

The crystalline quality of the single crystal samples was characterized by HRXRD. The x-ray maps produced by this technique are a plot of the x-ray intensity for omega, the sample angle, vs. omega/2 theta, the angular relationship normally used for x-ray analysis (see Figure 3.2). Essentially a standard omega-2theta x-ray diffraction scan is run repeatedly as the sample is rocked slightly off the normal omega angle. HRXRD maps are shown in figures 4.21 (as received), 4.22 (after Mn^+ implantation), 4.23 (after post implantation anneal) and 4.24 (after sputter).

The plot of the as received sample shows elongation of the x-ray pattern in the omega direction with a total angular divergence of 0.15^0 omega. It also exhibits asymmetry in the omega/2 theta direction with a total width of 0.05^0 omega/2 theta. After implantation with Mn^+ (185 eV, 5×10^{15} Mn^+/cm^2) the x-ray map (Figure 4.22) is spread out over more than 4^0 omega and 1^0 omega/2 theta, and exhibits significant asymmetry in both these directions. After the post implant anneal (Figure 4.23) the

x-ray pattern has regained its original characteristics, exhibiting a 0.15^0 omega divergence and improving its symmetry in omega/2 theta space. This sample also had a narrowed omega/2 theta angular distribution of 0.025^0. One of these single crystal samples was then subject to sputter by Ar^+ at 3 keV and 2×10^{-5} Torr and the x-ray map for this sample is shown in figure 4.24. The sputter x-ray map shows a diffuse pattern over 2.5^0 omega and 1.0^0 omega/2 theta angles with no discernible peaks. The central portion of the plot, which is distinguished from the outer fringes by a wide band of reduced intensity, forms a broad plateau with a full width at half maximum of 1^0 omega and 0.5^0 omega/2 theta.

Activator Efficiency Measurements

In order to separate changes in brightness due to activator effects from those attributed to changes in the host lattice, luminescent transients of both the as deposited and degraded (2 keV, 1×10^{-6} Torr oxygen, 120 C/cm^2, 3 nm oxide thickness) samples were measured. Figures 4.25 and 4.26 show the luminescent decay curves which are plots of relative intensity vs. time for as-deposited and degraded ZnS:Mn samples measured with a primary beam of 2 keV and 9 keV, respectively. The 9 keV plot which measures the full thickness of phosphor shows a very small (~0.5%) lower intensity for the degraded sample. The 2 keV plot (where the degraded material represents a large fraction of the excited volume) shows a larger (~5%) difference between the samples. However neither of these results are proportional to the ~50% loss of brightness observed in the degraded sample. In both of these experiments, the as deposited and

degraded samples exhibited much the same decay characteristics as shown by the similarity of the decay curves.

Secondary Ion Mass Spectrometry (SIMS)

SIMS was performed on the single crystal samples with degraded (2 keV, 1 x 10^{-6} Torr oxygen, 120 C/cm^2, 3 nm oxide thickness) and reference (non-degraded) regions on the same sample to act as an internal standard for comparison of the two areas. Mass surveys which show the secondary ion signal for each mass/charge value from 0 to 140 were taken from the surface of both regions and at the end of each sputter depth profile. Figures 4.27 and 4.28 show the surface surveys for a reference and degraded area, respectively. There are two major differences between these two surveys, the oxygen signal is larger and the carbon signal is smaller on the degraded area consistent with the AES data reported above. Figures 4.29 and 4.30 show the surveys performed at the bottom of the sputter crater for the reference and degraded samples, respectively. Although these both are taken from well below the region directly affected by the electron beam, both the oxygen and the carbon signals from the degraded sample are lower than the reference.

The most useful information obtained from SIMS analysis of these samples was from the sputter depth profiles. These profiles are shown in figures 4.31 and 4.32 which show the signal intensity vs. sample depth for a reference and degraded area, respectively. The oxide layer on the degraded sample is visible in the first few nm, (the high oxygen and low sulfur signal area) and the interface between the oxide and the ZnS

is taken to be the point where the sulfur and oxygen signals cross in figure 4.32. By using the time taken to sputter through the oxide layer on the degraded sample (33sec), assuming the oxide thickness to be 3nm (from Auger sputter depth profiles) and by measuring the depth of the sputter crater after analysis (350 nm) the sputter rate is found to be approximately 6nm/min. The Mn is conspicuously absent from these plots because the SIMS conditions were chosen to optimize the oxygen (O) sensitivity, which gave poor Mn sensitivity because of the difficulty in forming Mn

[Benninghoven et al. 1987].

Thermoluminescent (Glow) Curves

In order to investigate the nature of the traps in the phosphor material, several thermoluminescent experiments were performed. The resulting glow curves, which are a graph of relative cathodoluminescent intensity as a function of temperature, are plotted in figures 4.33 (reference non-degraded ZnS:Mn sample) and 4.34 (ZnS:Mn sample degraded at 2 keV, 1×10^{-6} Torr oxygen, 120 C/cm^2, 3 nm oxide thickness). The reference sample exhibits a single small peak about twice the noise level at -84^{0}C with a full width at half maximum of 25^{0}C. The degraded sample shows two peaks the first at -112^{0}C and the second, which is about twice as intense, at -60^{0}C this peak has a full width at half maximum value of 20^{0}C. The positions of these peaks on the temperature scale are characteristic of the type of trap formed in the material, and the full width at half maximum value gives an indication of the distribution of trap energies.
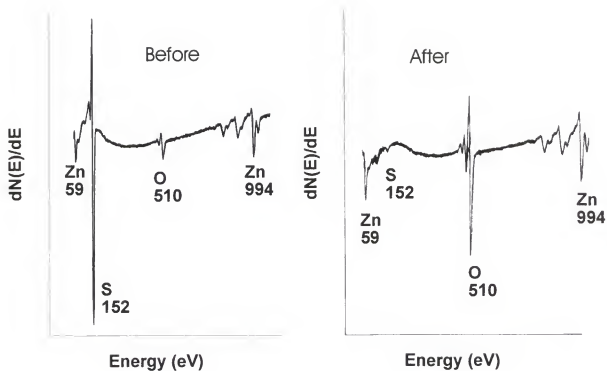
Figure 4.1.   AES spectra from ZnS sample both before (left) and after (right) electron beam bombardment at 2 keV in oxygen at 1 x 10⁻⁷ Torr to a terminal dose of 200 C/cm².
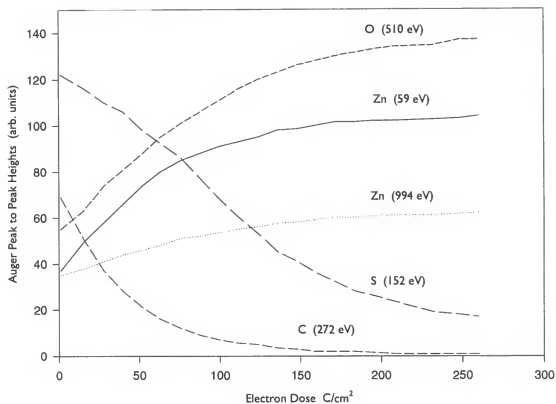
Figure 4.2.   Auger peak-to-peak heights vs. electron dose plotted for a ZnS:Mn
sample degraded at 4 keV in water vapor at 5 x 10⁻⁸ Torr.
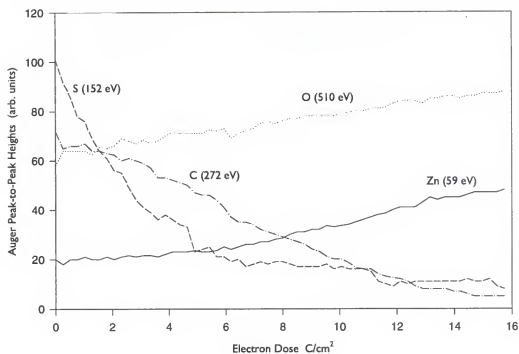
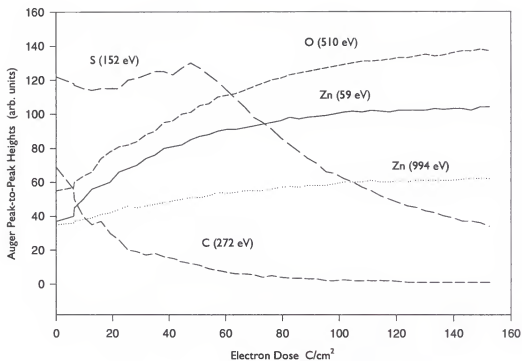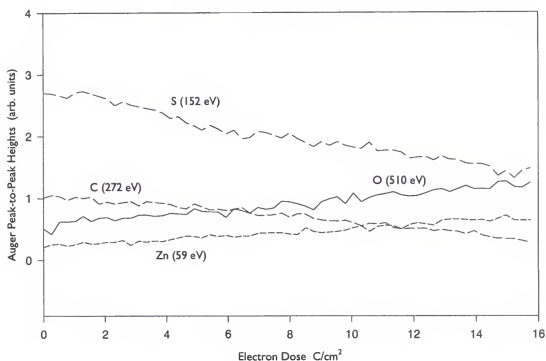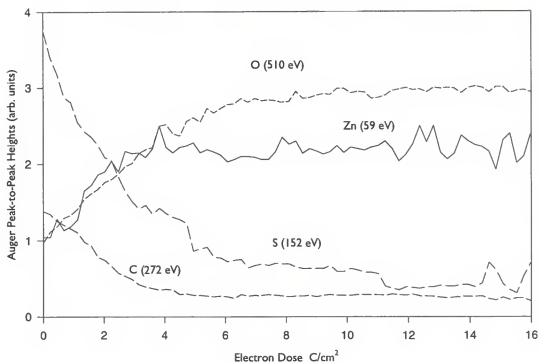Figure 4.3.   Auger peak-to-peak heights vs. electron dose during ZnS:Mn degradation at 1 keV in water vapor at 5×10^{-8} Torr.

Figure 4.4.   Auger peak-to-peak heights vs. electron dose for a ZnS:Mn sample degraded at 2 keV in water vapor at 5 x 10⁻⁸ Torr.
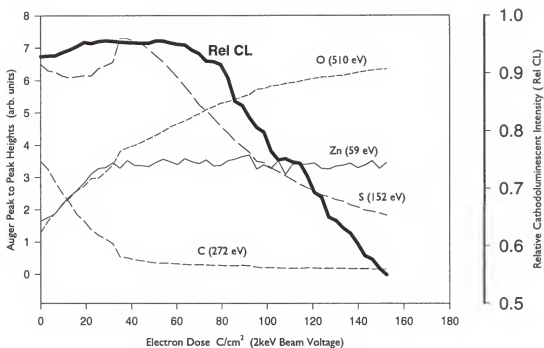
Figure 4.5.   Auger peak-to-peak heights vs. electron dose for a ZnS:Mn sample
                degraded at 1 keV in hydrogen at 1 x 10⁻⁶ Torr.
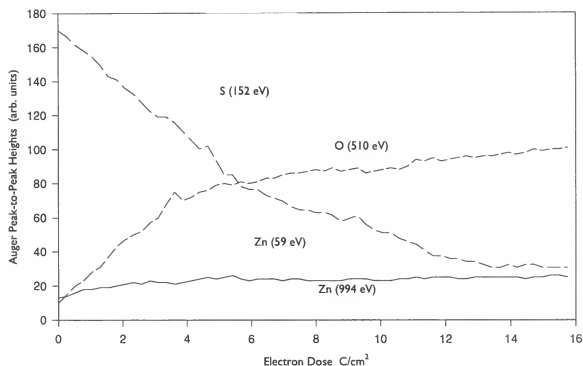
Figure 4.6.   Auger peak-to-peak heights vs. electron dose for a ZnS:Mn sample
degraded at 1 keV in oxygen at 1 x 10⁻⁶ Torr.
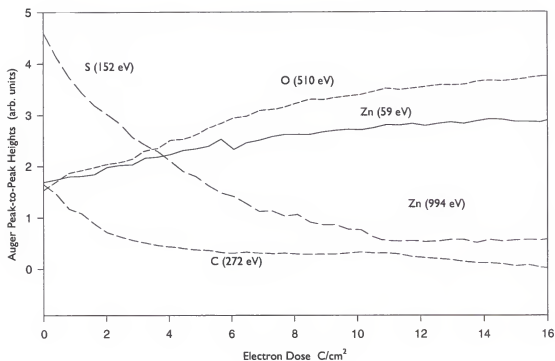
Figure 4.7.   Auger peak-to-peak heights vs. electron dose for a ZnS:Mn sample
degraded at 1 keV in a 1:1 mixture of hydrogen and oxygen at a total
pressure of 1 x 10⁻⁶ Torr.

Figure 4.8.   Auger peak-to-peak heights vs. electron dose for a ZnS:Mn sample degraded at 1 keV in water vapor at 1 x 10⁻⁶ Torr.

Figure 4.9.   Auger peak-to-peak heights and relative cathodoluminescent intensity collected simultaneously vs. electron dose for 2 keV and 5 x 10⁻⁸ Torr water vapor.
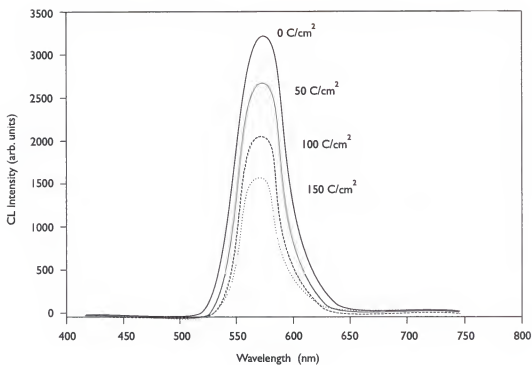
Figure 4.10.   Spectra of ZnS:Mn taken at 2 keV before and during degradation in oxygen to several Coulombic doses. Note the absence of any spectral shift during degradation.
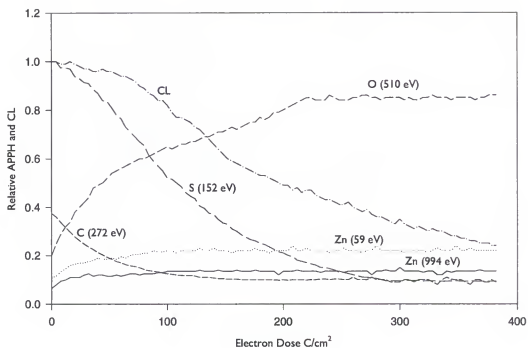
Figure 4.11.   Relative Auger peak-to-peak heights and cathodoluminescent data taken at 4 keV in oxygen at 1 x 10⁻⁶ Torr.
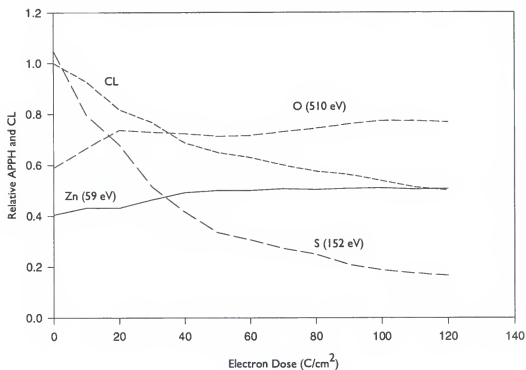
Figure 4.12. Relative Auger peak-to-peak heights and cathodoluminescent data taken at 2 keV in oxygen at 1 x 10⁻⁶ Torr.
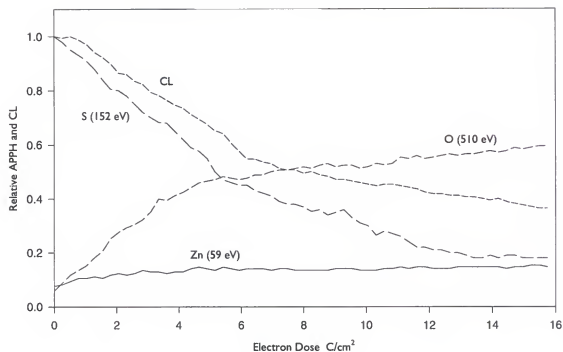
Figure 4.13. Relative Auger peak-to-peak heights and cathodoluminescent data taken at 1 keV in oxygen at 1 x 10⁻⁶ Torr.
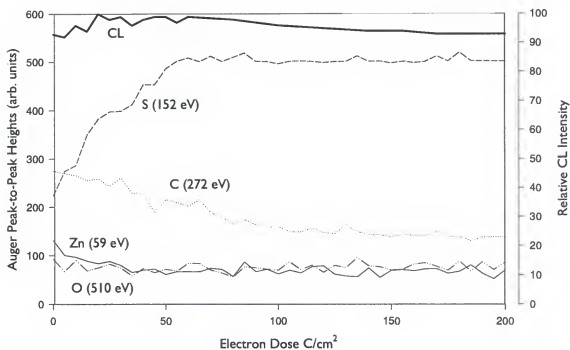
Figure 4.14.   Auger peak-to-peak heights and relative cathodoluminescent data taken
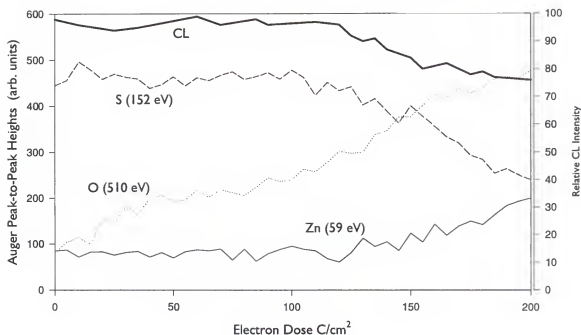at 2 keV in H$_2$S at 1 x 10^{-6} Torr.

Figure 4.15.   Auger peak-to-peak heights and relative cathodolminescent data for a sample previously bombarded with electrons in H_2S (see figure 4.12), degraded in oxygen at 2 keV and 1×10^{-6} Torr.
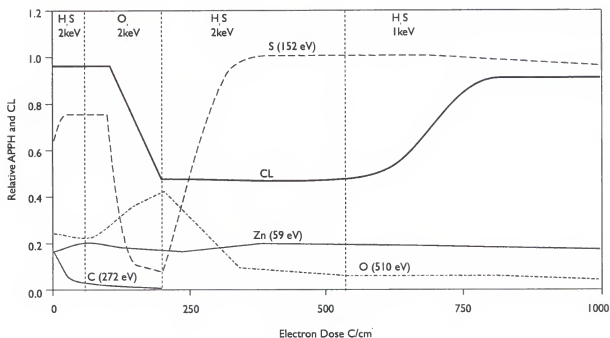
Figure 4.16.   Relative APPH and cathodoluminescent data for a ZnS:Mn sample
bombarded with 1 and 2 keV electrons. The sample was first bombarded
in H₂S at 2 keV, then degraded in oxygen at 2 keV, and finally re-exposed
to H₂S at 2keV and 1 keV. Note the CL brightness does not begin to
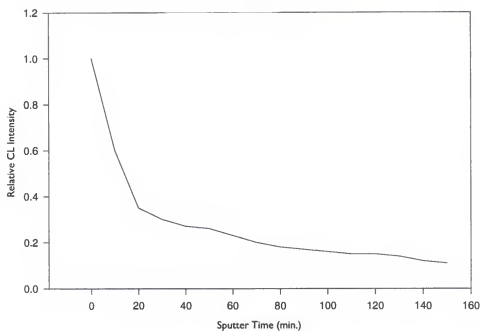recover until the primary beam voltage is reduced to 1 keV.

Figure 4.17. Plot of relative cathodoluminescent brightness vs. sputter time in 3 keV Ar⁺ for ZnS:Mn.
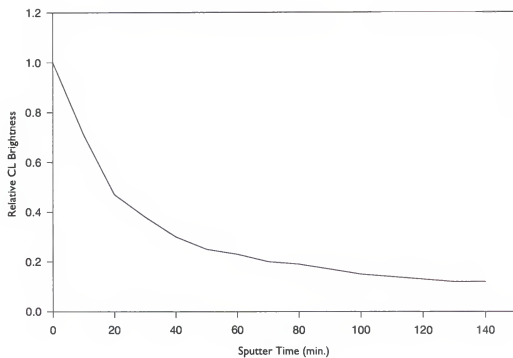
Figure 4.18. Relative cathodoluminescent brightness vs. sputter time in 3 keV Ar⁺ for ZnS:Mn single crystal sample.
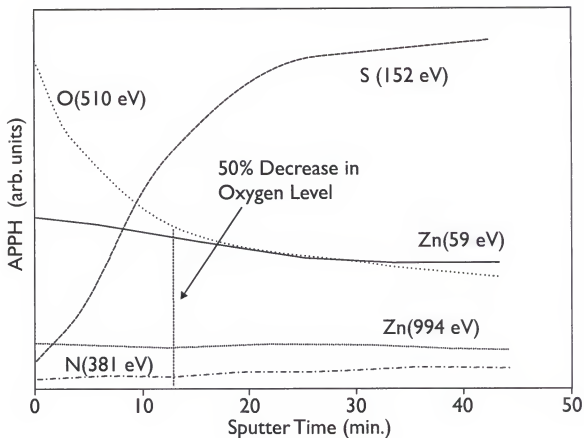
Figure 4.19. Example of plot data used to determine thickness of oxide layers on ZnS by sputter depth profiling. Sample was degraded at 2 keV in oxygen at 1×10^{-6} Torr to 120 C/cm². Dashed line indicates point where oxygen Auger signal has been reduced by 50%. This point is considered to be indicative of the ZnO-ZnS interface.
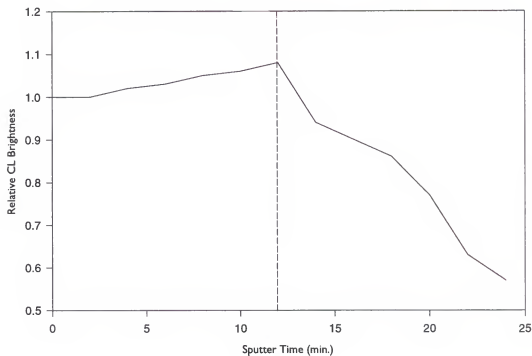
Figure 4.20.   Plot of sputter time vs. relative cathodoluminescent brightness for a
ZnS:Mn sample as the ZnO surface layer grown previously by electron
beam bombardment (2 keV in oxygen at 1 x 10⁻⁶ Torr to 120 C/cm²) is
removed by sputtering.
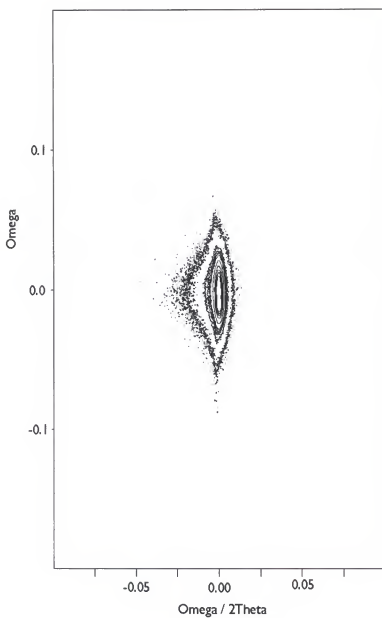
Figure 4.21. High resolution x-ray diffraction (HRXRD) x-ray map of single crystal ZnS sample as recieved.
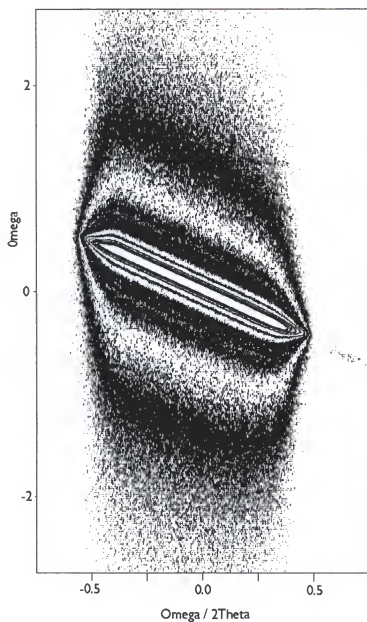
Figure 4.22.   High resolution x-ray diffraction (HRXRD) x-ray map of single crystal
ZnS sample after implantation with Mn⁺ at 185 keV, note the change in
plot scale from the as recieved plot.
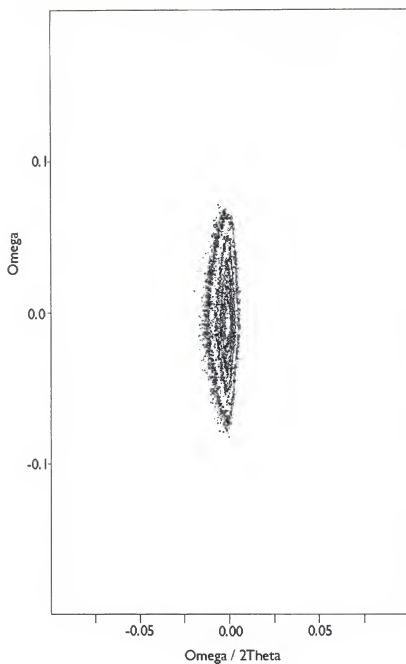
Figure 4.23.   High resolution x-ray diffraction (HRXRD) x-ray map of the single crystal ZnS sample after post implant anneal.
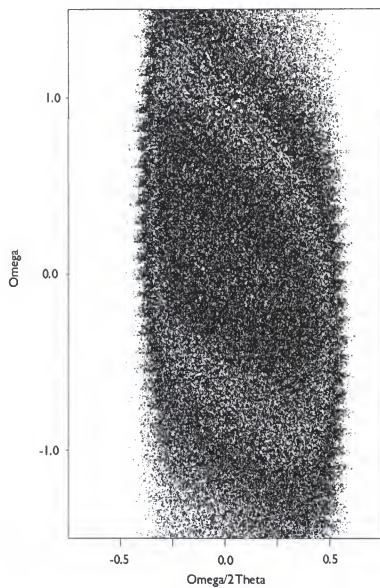
Figure 4.24. High resolution x-ray diffraction (HRXRD) x-ray map of the sputtered single crystal sample.
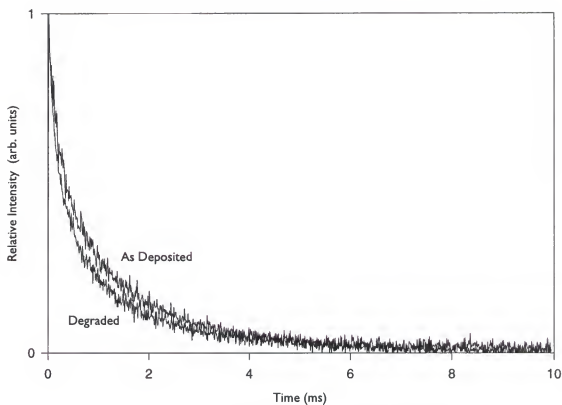
Figure 4.25.   Luminescent decay curves for ZnS:Mn degraded (bottom, degraded at 2
               keV in oxygen at 1 x 10⁻⁶ Torr to 120 C/cm²) and as deposited (top)
               samples measured with 2 keV electrons.
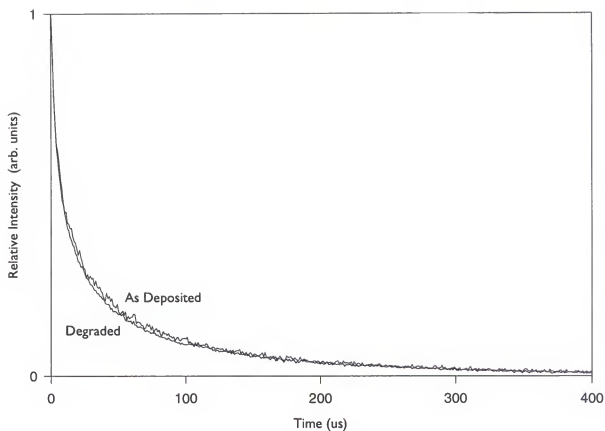
Figure 4.26.   Luminescent decay curves of degraded (bottom, degraded at 2 keV in oxygen at 1×10^{-6} Torr to 120 C/cm^2) and as deposited (top) ZnS:Mn measured with 9 keV electrons.
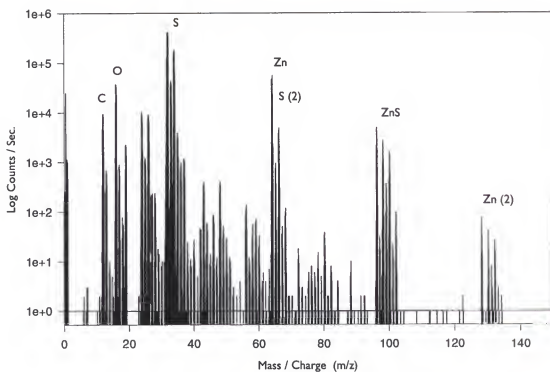
Figure 4.27.   Negative SIMS survey of ZnS single crystal prior to depth profile.
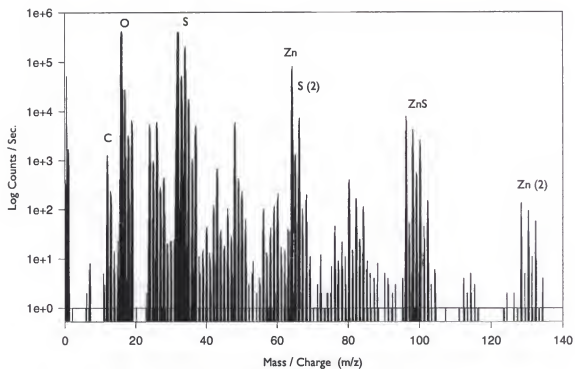
Figure 4.28. Negative SIMS survey of degraded area before depth profile. Sample was degraded at 2 keV in oxygen at 1 × 10⁻⁶ Torr to 120 C/cm².
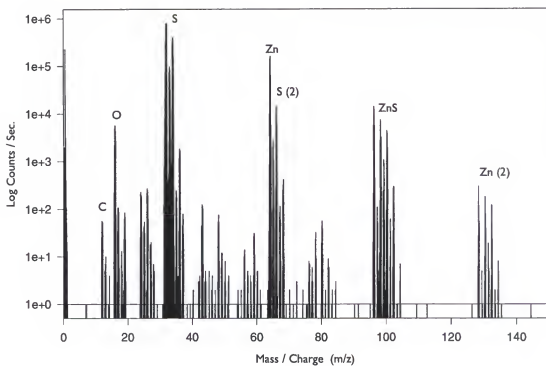
Figure 4.29.   Negative SIMS survey of ZnS single crystal sample after depth profile
(bottom of profile crater).
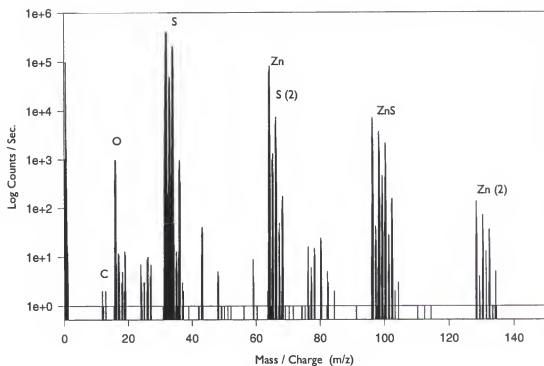
Figure 4.30.   Negative SIMS survey of degraded sample after depth profile (bottom of
                sputter crater). Sample was degraded at 2 keV in oxygen at
                1 x 10^{-6} Torr to 120 C/cm^2.
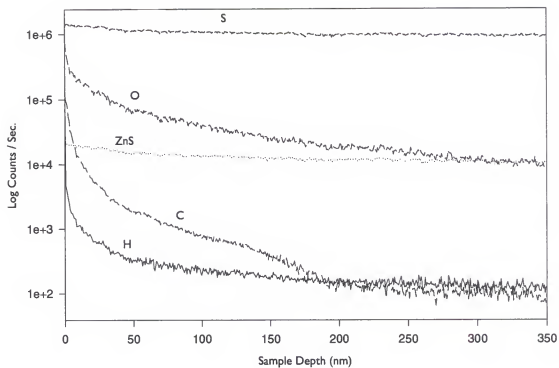
Figure 4.31.   SIMS sputter depth profile of ZnS single crystal reference sample.
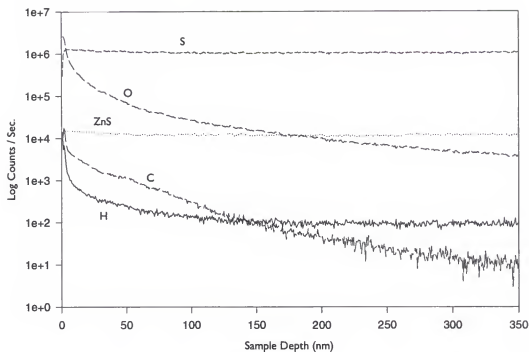
Figure 4.32.   SIMS sputter depth profile plot of single crystal sample degraded by 2 keV electrons in 1 x 10⁻⁶ Torr oxygen to 120 C/cm².
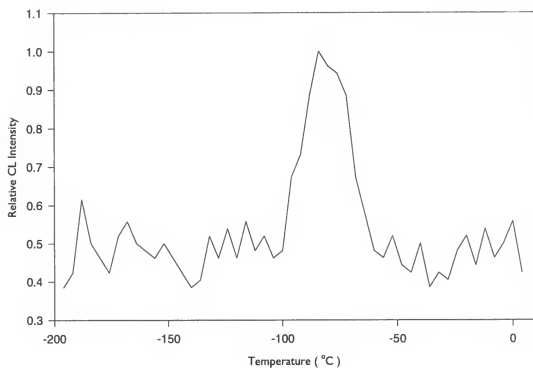
Figure 4.33.   Thermoluminescent (glow) curve for a non-degraded(reference)
                ZnS:Mn sample.
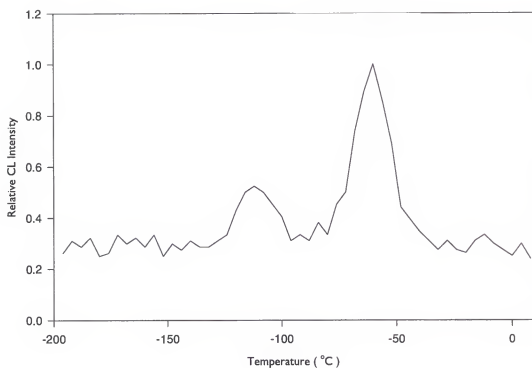
Fig 4.34.   Thermoluminescent (glow) curve for a ZnS:Mn sample degraded by 2 keV
             electrons in 1 x 10⁻⁶ Torr oxygen to 120 C/cm².

CHAPTER 5
DISCUSSION

As demonstrated by the data presented in chapter 4, ZnS phosphors degrade during electron beam bombardment. That is to say, during prolonged excitation at a constant current density, the brightness decreased with time. At low excitation voltages (< 2keV) the decrease in brightness proceeds so rapidly that ZnS phosphors do not have a useful service life. The sections that follow illustrate the connection between the surface chemical reactions, stimulated by the electron beam, that occur between the phosphor material and the vacuum ambient and the alterations these reactions produce in the physical structure of ZnS. These changes include the growth of an oxide layer on the surface of the phosphor and the diffusion of oxygen into the lattice near the surface. After accounting for the effects of the oxide layer, this work demonstrates that oxygen in the ZnS:Mn caused the observed loss of brightness.

Surface Chemical Reactions

Reactions on the surface of the ZnS were monitored using AES, which facilitated the collection of information about the progress of reactions on the characteristics of the surface, without the influence of the bulk material which remained unaffected.

112

While there are dependencies on experimental conditions that will be explained later, there are several general trends in the AES degradation experiments.

Figure 4.2 is an example of a typical degradation experiment, performed at 4 keV and 5×10^{-8} Torr water vapor. Over the course of the experiment, the zinc and oxygen signals increase simultaneously and appear to saturate after 150 C/cm^2. The concurrent changes of these two signals are consistent with the oxidation of the zinc during bombardment. Adventitious carbon, which was present from sample handling and exposure to the laboratory ambient environment, decreases in a generally exponential fashion from the beginning of the experiment. Sulfur remains constant or decreases slowly as carbon is being removed, but there is an increase in the rate of loss when most of the carbon signal has been lost. This trend suggests that there is a competing reaction on the surface between the sulfur and carbon, which will be addressed in some detail in a later section. The effect of these competing reactions are very evident in figure 4.4 for 2 keV electrons in 5×10^{-8} Torr water vapor, where the decline of the sulfur signal did not begin until the carbon signal is nearly zero. This figure also illustrates the surface sensitivity of AES. As the surface carbon is removed, the thickness of material through which the sulfur Auger electrons must travel before escaping the solid is reduced and the sulfur signal increases.

All of the above data are consistent with the electron beam dissociation of oxidizing residual gas molecules which lead to the formation of ZnO on the surface of the phosphor. However beyond this stimulation of surface chemical reactions, electron beams are known to often cause electron stimulated desorption (ESD) [Williams and de Segovia 1989, Madey and Yates 1971]. In this process ionized or neutral sulfur atoms

are desorbed because the primary electrons may cause ejection of bonding electrons, reducing the sulfur concentration on the surface of ZnS. This type of desorption would result in degradation when only the electron beam was present; no gas would be needed to observe degradation. However, samples bombarded at vacuum levels of 10^{-9} Torr or better, showed little (<1%) or no change in surface chemistry, or CL brightness for electron doses up to 200 C/cm^2. In addition, neither S$^-$ or S$^+$ were detectable from the sample during bombardment. This suggests that ESD is not the dominant factor in the surface changes. Furthermore, carbon and sulfur were not removed from the surface during exposure to oxygen without electron bombardment. Removal of carbon or sulfur was only observed during electron bombardment in the presence of a reactive ambient.

The observed behavior is consistent with the removal of both carbon and sulfur from the surface of the phosphor by an electron stimulated process (Figure 5.3). During this process, sulfur atoms on the surface are postulated to react with chemically active gas molecules or adsorbed atoms produced by electron beam cracking of residual gas molecules, as in

$$ZnS + H_2O \xrightarrow{e-} ZnO + H_2S(\uparrow) \qquad (5.1)$$

or similarly

$$ZnS + (X+1)H_2O \xrightarrow{e-} ZnO + SO_x + (X+1)H_2 \qquad (5.2)$$
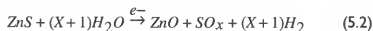
The reaction products (SO$_x$ or H$_2$S) have high vapor pressure and volatilize from the surface of the phosphor. Carbon could be removed by a similar reaction, i.e.,

$$C + (X)H_2O \xrightarrow{e-} CO_x + (X)H_2 \qquad (5.3)$$
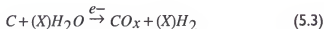
and the H$_2$ and CO or CO$_2$ that forms would also quickly desorb from the surface into the vacuum ambient.

In addition, it is clear from the AES data that as the sulfur is removed from the surface and replaced by oxygen, a thin ZnO layer forms on the surface. If this ZnO were a non-luminescent or "dead" layer, it could interfere with the underlying phosphor material by attenuating the incoming electron beam and by absorbing light as it travels through the layer, both of which can lower the observed brightness of the phosphor. These and other issues plus the dependence of degradation on changes in the experimental conditions are discussed below.

Modeling of the Electron Stimulated Surface Reaction

In the proposed model for the electron stimulated surface reaction (ESSR, figure 5.1) it is postulated that a molecule adsorbs on the surface of the phosphor from the vacuum ambient. The electron beam ionizes the molecule by ejection of bonding electrons causing it to dissociate into its atomic or molecular components which are highly reactive. In the case of oxygen or hydrogen, atoms react with a surface sulfur atom from the ZnS to form volatile compounds, as shown in equations 5.1 and 5.2 these

reaction products desorb from the surface and leave zinc atoms with dangling bonds. Additional molecules may adsorb from the vacuum (in this case oxygen or water) and before or after dissociation, bond with the unsatisfied zinc atoms to form a surface layer of ZnO.

To mathematically describe this process, let C_s be the concentration of sulfur atoms on the surface of the phosphor before degradation begins. Then the change in concentration during the experiment can be expressed as

$$dC_S/dt = -kC_S C_{as}^n \qquad (5.4)$$

where k is the reaction rate constant between sulfur and the adsorbed atomic species (e.g. oxygen), n is the order of the reaction, and C_{as} is the concentration of adsorbed atomic species given by

$$C_{as} = Z\phi_{m-a}C_m J \qquad (5.5)$$

where ϕ_{m-a} is the cross section for the electron dissociation of molecular to active molecular or atomic adsorbed species, C_m is the concentration of adsorbed molecular species, and J is the electron flux on the surface. Z is the sum of the atomic subscripts in the molecule (i.e., for $O_2 \to 2O$, Z is 2). C_m can be further expanded to illustrate its dependence on pressure P_m from ideal gas adsorption behavior [Redhead et al. 1968]

$$C_m = (\tau_0 e^{Q/RT}) \frac{P_m}{(2\pi mkT)^{1/2}} \qquad (5.6)$$

where τ_O is the inverse of the escape attempt frequency, Q is the desorption energy, m is the gram molecular weight, T is the temperature and P_m is the partial pressure of the molecular species. Then by substituting equation 5.5 into equation 5.4 we have

$$dC_S/dt = -kZC_S(\phi_m - aJ[\tau_0 e^{Q/RT}\frac{P_m}{(2\pi mkT)_{1/2}}]^n \quad . \quad (5.7)$$

To collect constants, let

$$K^I = k(T)Z\phi_m - a(E_p)[\tau_0 e^{Q/RT}(2\pi mkT)^{-1/2}]^n \quad (5.8)$$

then (5.7) becomes

$$dC_S = -K^I J[Pm]^n C_S dt \quad (5.9)$$

Integrating with respect to time yields

$$C_S = C_S^0 \exp(-K^I [P_m]^n Jt) \quad (5.10)$$

where Jt is the coulombic dose and C_S^0 is the sulfur surface concentration at t = 0. It follows that the concentration of sulfur atoms on the surface (C_s) should decay exponentially from the original surface concentration ($C_s°$) with coulombic dose

(coulombs/cm^2). For a fixed extent of reaction, the time required to remove a fixed amount of sulfur from the surface should decrease linearly as the pressure (P_m) is increased if the reaction is first order.

Figure 5.2 is a plot of relative Ln sulfur APPH in oxygen at pressures from 1×10^{-6} to 5×10^{-8} Torr vs. degradation time in minutes. This figure shows a linear dependence of the Ln sulfur APPH with time, indicating the expected exponential dependence of the amount of sulfur on the surface of the phosphor with time. The change in slope visible in the lower four pressures demonstrates the protective effects of carbon on the surface of the phosphor. The rate of sulfur depletion is significantly reduced until the carbon has been desorbed, at this point the rate of sulfur depletion increases as demonstrated by the increase in the slope of the Ln sulfur APPH lines. Figure 5.3 shows a plot of the time it takes the ZnS sulfur APPH to reach 50% of its original intensity (time to a fixed extent of reaction, from figure 5.2) in oxygen at different pressures. The plot is linear over one and a half orders of magnitude, suggesting first order dependence of the surface chemical reaction that removes the sulfur.

Effect of the Vacuum Ambient

Figure 5.4 is a summary of the relative sulfur APPH (taken from figures 4.5, 4.6, 4.7 and 4.8) for samples degraded at 1 keV in 1×10^{-6} Torr of hydrogen, oxygen, a 1:1 mixture of hydrogen and oxygen, and water vapor. Although both hydrogen and oxygen cause degradation separately, both the gas mixture and water vapor are more

effective than either molecule alone. Water vapor caused a faster decline in the sulfur APPH than the 1:1 mixture of hydrogen and oxygen at the same pressure. This change in sulfur removal for different vacuum ambients can be attributed to differences in the size and adsorption mechanism of the molecules.

The probability that an electron will strike an adsorbed molecule is roughly proportional to its area [Redhead et al. 1968], therefore larger molecules will have a greater probability of conversion from molecular to atomic species [Kaminski 1965]. In this case H_2 is the smallest molecule then O_2 and H_2O the largest. The data follow a similar pattern with hydrogen producing the lowest rate of degradation, water vapor the greatest rate, and the rate of oxygen in between. In addition, hydrogen and oxygen rely on van der Waals bonds to adsorb on the surface, while water forms a hydrogen bond. Because the hydrogen bond is stronger (15 kcal/mole vs. 5 kcal/mol for van der Waals) the water will have a longer mean stay time on the surface further increasing the probability of conversion to atomic species [O'Hanlon 1989]. In the case of hydrogen, the cross section for conversion from molecular to atomic species is four orders of magnitude smaller than oxygen [Nishijima and Propst 1970] which reduces the rate of hydrogen atom production, and limits the rate of the surface reaction.

The ESSR reaction has also been observed for other gas species. Figure 4.14 shows APPH and CL data for a ZnS sample bombarded with 2 keV electrons in H_2S at 1×10^{-6} Torr. The sulfur signal increases steadily until 50 C/cm^2, where its signal appears to saturate, and remains constant for the remainder of the experiment. These results are consistent with the cracking of the H_2S by the electron beam, which deposits sulfur on the surface of the ZnS. Similar results have also been reported for CO and

CO_2 which cause both desorption of sulfur and deposition of carbon during electron bombardment [Darici and Holloway 1997].

While equation 5.10 predicts an exponential dependence of the sulfur and oxygen signals with electron dose, the attenuation of Auger electrons in layers thicker than the escape depth could also result in exponential dependencies of these peaks heights versus electron dose. Previous research [Swart et al. 1996] has shown that saturation of the oxygen AES signal versus electron dose was in fact due to the limited escape depth of Auger electrons from the sample, and that the thickness of the layer continued to increase after saturation of the AES signal was observed. The possibility of sulfur signal saturation was investigated in figure 5.5, by plotting the relative CL intensity versus relative sulfur APPH during electron bombardment with 4 keV primary electrons in oxygen at 1×10^{-6} Torr. The linearity of figure 5.5 at low relative sulfur APPH (toward the end of the experiment, when there was an oxide layer on the surface) indicates that the exponential behavior was in fact real, and not a result of sulfur signal attenuation by the oxide layer.

The ESSR deposition of sulfur has also been shown to delay the onset of degradation in ZnS:Mn. Figure 4.15 shows the APPH and CL vs. electron dose for a sample previously sulfidated (Figure 4.14) which has been degraded in oxygen at 1×10^{-6} Torr with 2 keV electrons. The decrease of both the sulfur and CL signals does not occur until 120 C/cm^2, whereas this decrease would have normally started at 30 C/cm^2 or less for an untreated sample. This behavior is attributed to the ESSR removal of excess surface sulfur before sulfur is removed from the bulk material. It is also likely that the deposited sulfur reduces the number of available molecular adsorption sites,

further reducing the degradation by limiting the production of atomic species. Molecular species must adsorb on the surface before they can be converted by electron bombardment into active atomic species.

<u>Effects of Primary Beam Energy</u>

The effect of primary beam energy on the change of surface chemistry is shown in figure 5.6 where the relative sulfur APPH vs. electron dose for 1, 2, and 4 keV primary beam energies, from figures 4.3, 4.4, and 4.2, respectively, is plotted for water vapor at a pressure of 5×10^{-8} Torr. As the primary beam voltage is reduced, the decrease of the sulfur APPH becomes more and more rapid. At 1 keV the coulombic load to reach 15% of the original APPH is one tenth the dose required for the same decrease at 2 keV and less than one fifteenth the dose required at 4 keV. This effect is consistent with both an increase in the dissociation cross-section for the molecular species, with a consequent increase in the electron stimulated surface reaction rate as the primary beam energy is reduced [Redhead et al. 1968]. Similar dependencies of ionic desorption cross sections [Moore 1961, Redhead 1964, Coburn 1968], electron stimulated desorption cross sections [Menzel and Gomer 1964, Nishijima and Propst 1970] and gas phase ionization efficiencies [Massey and Burhop 1952] have been demonstrated. In general the maximum rate of conversion from molecular to atomic species occurs in the range of 100-300 eV, with peak rates more than two orders of magnitude larger than the high energy (> 5 keV) rates. These results suggests the rate of the ESSR should follow a similar voltage dependence, and this conclusion is consistent

with the data over the 1-4 keV primary beam voltage range. In addition, the dependence of the relative CL brightness on primary beam voltage is depicted in figure 5.7, which shows CL brightness vs. coulombic dose for samples bombarded with 1, 2, and 4 keV primary electrons in 1×10^{-6} Torr of oxygen. These similarity of the data in figures 5.6 and 5.7 strongly suggest that the reduction of the CL brightness during bombardment can be correlated with the ESSR.

Further evidence of this energy dependence is shown in figure 4.16, in which a ZnS:Mn sample is sulfidated in H_2S, degraded in oxygen and resulfidated in H_2S. The primary beam energy is 2 keV until 520 C/cm^2 where it was reduced to 1 keV. During resulfidation from 200 to 520 C/cm^2 at 2 keV, the sulfur APPH increases from 0.1 to 1.0 and saturates at this value. The CL brightness however does not change, remaining at 0.5. Shortly after the primary beam voltage is reduced to 1 keV at 520 C/cm^2, the CL brightness begins to increase and by 750 C/cm^2 has stabilized at 0.9. While the details of the mechanism of this recovery of CL brightness are at this time uninvestigated, the voltage dependence of this data are consistent with the previous results.

Dependence of Cathodoluminescence on Surface Chemistry

Changes in the brightness of the phosphor film can be correlated with the changes in the surface chemistry. Auger and cathodoluminescent data are shown in figure 4.9 versus coulombic loading, both collected concurrently for 2 keV electrons in water vapor at 5×10^{-8} Torr. The CL brightness of the phosphor film was stable as long

as the protective carbon contamination was present. This behavior suggests that the reaction rate constant for carbon is much larger than the rate constant for sulfur at 2 keV, and therefore dissociated species on the surface preferentially react with the carbon which protects the phosphor from degradation as long as it remains on the surface. However, once the carbon was removed by a dose of 40 C/cm^2, the sulfur signal declined with a corresponding decrease in the cathodoluminescent brightness. This behavior is also consistent with the postulate that carbon was a surface contaminant layer, covering the ZnS and reducing the CL brightness and sulfur APPH.

There are at least three aspects of the phosphor that could account for these changes in brightness. The first is the oxide layer formed on the surface, which could attenuate the primary electron beam as it enters the solid reducing the power available to the underlying luminescent material. This layer could also absorb the light produced within the phosphor material as it travels through the oxide layer. The second possibility is that the surface chemical reaction affects the luminescent centers in the phosphor system, in this case the Mn^{+2} ion, and reduces its radiative efficiency or wavelength of emission by changing the local crystal conditions around the Mn. Finally, the ESSR reaction could induce changes in the phosphor matrix, ZnS, and increase the host losses which would reduce the rate of luminescent center excitation, presumably by a high rate of nonradiative recombination in the host.

Surface Layer Effects

The ZnO layer which forms during degradation creates a non-luminescent or "dead" layer [Swart et al. 1996] over the phosphor which should both attenuate the

power delivered by the electron beam to the phosphor and change the absorption of light radiating out of the phosphor. In addition, ZnO and ZnS may have different secondary electron emission coefficients and these coefficients are a function of the primary beam energy. This coefficient represents the ratio of the number of secondary electrons emitted from the material divided by the number of incoming primary electron, i.e., a coefficient of one indicates that one secondary electron will be emitted for each primary electron incident on the material [Readhead et al. 1968]. If the number of secondary electrons emitted from the material changes significantly during degradation, the surface charge state of the material would also change. This state of surface charge can drastically alter both the interaction of the primary electron beam with the sample, and the distribution of electrons and holes within the material [Sze 1981]. Each of these effects would change the brightness of the phosphor system and all therefore warrant investigation.

X-Ray Photoelectron Spectroscopy (XPS)

Although the concurrent increase in the oxygen and zinc peaks during AES indicated the formation of ZnO, XPS analysis was performed at the University of the Orange Free State in South Africa [Oosthuizen et al. 1997] to determine the chemical bonding of the surface layer. XPS analysis was performed on a ZnS powder sample both before and after degradation. Because XPS is much more sensitive to the shifts in emitted photoelectrons due to the bonding state of the atom, it is possible to differentiate between zinc bonded to oxygen and zinc bonded to sulfur or sulfate.

Figure 5.8 shows XPS spectra of the Zn 2p peaks for ZnS before and after degradation, compared with a reference ZnO spectra. There is a clear shift in this peak from 1023.3 eV before degradation presumably due to ZnS, to 1021.9 eV after, which corresponds to the Zn 2p peak in the reference ZnO sample. Figure 5.9 is a similar XPS spectra comparing the oxygen signal in the ZnO reference sample to the oxygen signal in the degraded ZnS sample. Again there is good agreement in both peak position and shape between the two spectra. This indicates the oxygen in the degraded ZnS is bonded in a similar manner as the oxygen in the ZnO standard. XPS from $ZnSO_4$ has also been reported [Nefedov 1982] and indicate the Zn 2p peak would be expected at 1023.1 eV; this peak is not visible after degradation. Both of these results indicate the surface layer is ZnO, and further analysis could be based on this fact.

Effects of ZnO Layer on CL Brightness

Possible brightness changes due to optical absorption were ruled out in three ways. First the damping constant (k) for ZnO was calculated from a high purity ZnO sample of known thickness (see Appendix A). This constant was then used to calculate the light absorption of the 3 nm of oxide typically present after degradation. These calculations indicate that 0.7% absorption should be expected for an oxide of this thickness. In addition, measurements of CL brightness from a ZnS:Mn thin film sample which had been sputter coated with 125 nm of ZnO showed only a 16% reduction in brightness between the coated and uncoated areas. Neither of these data could account for the 50% observed loss of CL brightness. Finally, any significant optical

absorption would have shown the degraded region as a dark spot on the surface of the phosphor, which was not observed. Having eliminated optical absorption as a major factor in the loss of brightness, both attenuation of the electron beam and changes in the state of surface charge remained as possible surface layer factors.

The two remaining surface layer effects, attenuation in the oxide layer and changes caused by the charge state of the surface, are difficult to differentiate from each other. Previous research [Swart et al. 1997] concluded that 13 nm of ZnO or more would be necessary for significant (~50%) attenuation of the primary beam. Another researcher [Seager et al. 1997] has shown the complexity of accurately modeling the distribution of charge near the surface, and the difficulty of predicting the effects of this charge distribution on the primary beam and carriers generated within the material. While the effects of surface charge on the overall brightness of the system were not investigated, it was necessary to demonstrate that the effect of the oxide layer on surface charge did not appreciably change the luminescent characteristics of the material.

To investigate the effects of the surface layer on CL brightness, the ZnO layer formed during degradation in oxygen was removed by sputtering with 3 keV Ar$^+$, while the CL brightness of the sample was monitored. Figure 4.17, a plot of relative CL intensity vs. sputtering time, shows the effects of sputtering on an as-deposited ZnS:Mn thin film sample. The brightness of the film begins to decrease immediately after sputtering is started and drops to about 30% relative brightness during the first 20 minutes of sputtering. In order to investigate this effect further a single crystal ZnS:Mn sample was sputtered under the same conditions. Figure 4.18 shows the relative CL

brightness vs. sputter time for this sample, and the results are nearly identical to the thin film. The single crystal was then analyzed with HRXRD and these results are plotted in figure 4.24 as an x-ray map of omega vs. omega/2 theta. When the post sputter x-ray map is compared to the map before sputter (Figure 4.23), it is clear that significant damage has been done to the surface of the sample. The X-ray pattern after sputter has been spread over more than two degrees of omega and a full degree of omega/2 theta. There is also no distinct x-ray peak, but rather a large plateau of intensity in the center of the map. This pattern indicates that the surface of the sputtered sample is either polycrystalline or amorphous [Cullity 1978]. It is clear from these results that in addition to removing surface atoms the energetic Ar^+ ions will penetrate into the film and disrupt the crystal structure by causing point and extended defects, which reduced the overall efficiency and brightness of the film. This change in brightness was used to identify the ZnO/ZnS interface in subsequent sputter experiments.

The changes in relative CL brightness during sputtering of a ZnS:Mn sample previously degraded in oxygen to form a 3 nm ZnO surface layer are shown in figure 4.20. During sputter of the oxide layer the brightness increased slightly (~8%), however, once the sulfide interface is reached the brightness declines rapidly. It is likely some of the energetic Ar^+ penetrated the oxide and began to reduce the brightness of the ZnS before the oxide layer was completely removed, reducing magnitude of the observed brightness increase. However, both the abrupt change in the luminescent behavior at the interface and comparison of the brightness decrease with the other sputter data (Figure 4.18) suggest that the magnitude of this effect is small (<10%).

These results suggest that the combined effects of the oxide layer (optical absorption, primary beam attenuation and changes in the state of surface charge) can only account for an 8% decrease in CL brightness during degradation. This decrease in brightness is not sufficient to account for the 50% loss of brightness during the formation of the oxide layer. In addition, because the energy value of the Auger peaks are, in general, sensitive to the state of surface charge, a change in charge state would have been indicated by an energy shift of the Auger peaks [Holloway 1980]. Although small energy shifts did occur (2-3 eV) the data suggest that these shifts did not produce a significant effect on the observed CL brightness. Clearly one of the two remaining possibilities, changes in the luminescent center or a change in the host lattice, must be the dominant effect.

The Luminescent Center Mn^{+2}

The next logical place to look for brightness loss in the phosphor is at the luminescent center, in this case on the Mn^{+2} ion within the ZnS matrix. This phosphor is of the bandgap type, which means the luminescent ion produces localized energy levels within the bandgap of the host material [Blasse and Grabmaier 1994]. It is the electronic transitions between these levels that produce the luminescence from the system. Ions in bandgap luminescent systems are generally very sensitive to the local chemical environment, or crystal field, and the same ion in different hosts may produce different wavelengths of light. For example, Mn^{+2} in ZnS produces a broad band yellow emission (octahedral coordination, strong crystal field) while the same ion in Zn_2SiO_4

(tetrahedral coordination, weak crystal field) gives a broad band green emission. This sensitivity to crystal field can be used to determine when changes in the host lattice have occurred near the luminescent ion.

Figure 4.10 shows the emission spectra from a ZnS:Mn sample before degradation, and at several coulombic loadings during degradation. The intensity of the peaks decreases as the coulombic load increases, but the shape and position of the curve remained the same. This trend strongly indicates that the Mn^{+2} ion experienced the same crystal field in each case, which established that the local chemical surroundings of the ion did not change during degradation.

Another possibility is that the efficiency of the luminescent center is changing during degradation. This change would be manifest as a change in the time constant of the decay curve when a degraded sample was compared to an as deposited sample. Figure 4.26 and 4.25 show the luminescent decay curves (relative brightness vs. time) at 9 keV and 2 keV primary beam energy, respectively, of a ZnS:Mn sample degraded at 2 keV in oxygen. The higher energy 9 keV experiment will sample deep into the material (~0.5 μm) measuring both the degraded surface layer and the unaffected bulk material below. The 2 keV experiment should sample the phosphor to a depth of approximately 60 nm, which corresponds to the same region from which a drop to 50% of the original intensity had been observed. Therefore, the luminescent behavior of this region should be dominated by the phosphor material near the surface. The decay time constants for the 9keV degraded and as deposited samples are almost identical, which suggests the bulk of the phosphor is relatively unaffected by the surface reaction. The 2keV transients show a 5% difference between the two samples, indicating a 5%

reduction in total lifetime. Assuming that the radiative lifetime is constant, a 5% decrease in the total lifetime corresponds to a 5% reduction in activator efficiency (equation 2.6), and a corresponding reduction in external radiant efficiency (equation 2.7) in the degraded surface layer.

Although a 5% decrease in efficiency is measurable, it does not explain the 50% overall loss of brightness observed during degradation of the phosphor. This indicates that a change in the activator ion is not the dominant mechanism responsible for the loss of brightness observed. In addition, the combination of oxide layer and activator effects can account for at most a 13% change in the CL brightness from the sample. Having eliminated these two factors, the results point to a change in the host lattice as the dominant source of brightness loss.

<u>Changes in the ZnS Host Lattice</u>

In order to eliminate as many variables as possible from the host lattice investigation, ZnS single crystal samples were studied in addition to the thin film samples. Figure 4.21 is a HRXRD x-ray map of the crystals as they were received. On this type of map a perfect single crystal would show a symmetric circle. The asymmetry in the omega/2theta space indicates a deviation from the central lattice spacing value. In other words the strain across the crystal is not uniform, which deforms part of the lattice and changes the unit cell spacing for the strained area. The broadening over the omega space indicates crystallite misorientation, commonly referred to as mosaic structure (Figure 5.10). This structure is formed by the slight mistilt of neighboring

crystallites which reorient themselves to accommodate lattice defects such as dislocations. While this broadening indicates the as received crystal is not perfect, the full width at half maximum intensity is less than 0.1^0 omega, which indicates a high quality crystal. Figure 4.22 is a similar x-ray map of the crystal after ion implantation with Mn. This map covers more than 200 times the omega vs. omega/2theta space of the as received x-ray plot (note the difference in scale between the two plots) and the broadening in both the omega and the omega/2theta space shows the extent of the damage done during implantation, which is manifest both as a large distribution of crystallite misorientations and a significant amount of strain in the crystal. There was no measurable CL brightness from the sample in this condition, which is not unusual. Ion implanted samples are typically annealed after implantation to recover lattice damage and activate the dopant atoms [Kalkhoran et al. 1994]. The damage is recovered after annealing in hydrogen sulfide (Figure 4.23) which is plotted on the same scale as the as received sample. The full width at half maximum value in omega space is almost identical to the as received sample and the asymmetry in omega/2theta space is absent, suggesting the strain in the crystal has been eliminated. This analysis insured the single crystal samples fully recovered from the lattice damage induced during implantation, and were similar in crystal quality to the samples as received. A portion of each of these single crystal samples was degraded in oxygen to form 3 nm of ZnO on the surface, and this procedure produced samples with both degraded and nondegraded reference areas for analysis. These samples were then subject to SIMS analysis to determine differences in the chemistry between the two areas, and thermoluminescent measurements to characterize differences in their trap structures.

Figure 4.31 and 4.32 show the SIMS sputter depth profile plots of Log counts/sec. vs. sample depth time for the reference and degraded samples respectively. In both plots there is a strong and steady sulfur signal from the matrix and both hydrogen and carbon surface contamination that disappear into the noise level after 30 minutes of sputtering. The oxide layer is clearly visible in figure 4.32 as the first few nm of sample depth, and the interface between the oxide and sulfide is taken to be the point where the sulfur and oxygen profile lines cross. In order to accurately compare the signals between the two samples, the oxygen, carbon and hydrogen signals were normalized to the matrix (sulfur) signal for both samples and these results are plotted in figures 5.11 (reference) and 5.12 (degraded) as Log counts/sec of O/S, C/S and H/S vs. sputter time. When viewed separately the differences in the signal levels of these two graphs is not immediately evident, so both the degraded (dotted lines) and reference (solid lines) samples have been plotted together in figure 5.13.

Comparison of the normalized oxygen signals in figure 5.13 shows that the oxygen content of the degraded sample is significantly larger than the reference (non-degraded) sample until approximately 51 nm of sample depth. Both the hydrogen and carbon signals of the degraded sample are lower after the first few nm as compared to the reference sample, which is consistent with a reduced amount of carbon contamination on the surface of the degraded sample due to ESSR removal. A similar process for hydrogen would be reasonable, although it was not quantified in this study.

The differences in the oxygen content of the first 51 nm of the degraded and reference samples indicates that oxygen is being incorporated into the ZnS lattice in this region of the sample. Because the penetration distance of primary electrons at 2 keV is

on the order of 60 nm, the majority of the luminescence in the degraded sample at 2 keV is from the region of oxygen incorporation. The structure of ZnS is either zinc blende with a cubic close packing of the sulfur atoms (Figure 5.14), wurtzite (Figure 5.15) or a polytype combination of both [Kingery et al. 1976]. The single crystal samples were zinc blende (cubic) while the thin film samples were wurtzite (hexagonal) with some polytype incorporation of the cubic phase. Because no significant difference in degradation behavior was observed between the two types of samples, the behavior of oxygen is assumed to be insensitive to the ZnS crystal phase. It is unlikely the oxygen atoms would occupy interstitial sites in either structure because substituting on sulfur vacancies, resulting from sulfur diffusion to the surface and removal by ESSR, would produce a lower free energy configuration in the crystal [Kingerly et al. 1976]. Sulfur and oxygen have the same charge so this substitution would be isoelectronic with respect to the overall charge state of the crystal. Isoelectronic substitutions have been shown in the literature (see chapter 2) to form very efficient trap states in the bandgap of the host material. This particular substitution of oxygen on a sulfur site has been demonstrated to form an electron trap which is identified by its glow peaks at -100^0C and -50^0C in ZnS [Kroeger and Dikhoff 1952]. The most thoroughly characterized method to investigate the trap structure of wide bandgap luminescent materials is to use thermoluminescence.

Figure 5.16 shows the results from thermoluminescent or glow experiments performed on both a reference (non-degraded) and degraded ZnS:Mn single crystal sample. The peak in the glow curve at -84^0C from the reference sample is consistent with traps formed by sulfur vacancies (V_s) [Bryant and Hamid 1970] or sulfur Frankel

(V_s + I_s) disorders [Smith 1948], both of which exhibit glow peaks between -80°C and -90°C in ZnS. This peak has been suppressed in the degraded sample and instead peaks centered at -110°C and -60°C are evident. These peaks indicate the formation of traps in the degraded material by oxygen [Kroeger and Dikhoff 1952, Hoogenstraaten 1958], and the reduced intensity of the reference (V_s) peak suggests the oxygen is occupying sulfur sites in the lattice. This site would be the lowest energy configuration for the oxygen in the host lattice [Kingery et al. 1976]. In addition oxygen has been shown to diffuse through ZnS by hopping on sulfur vacancies [Shalimova et al. 1976] which provides further evidence that oxygen would preferentially occupy sulfur vacancies. Because the area between the two oxygen peaks does not return to the initial noise level, it is likely that some of the original sulfur defects remain in the degraded sample. The defects that remain are most likely to be Frankel type which are electrically neutral and should have a lower free energy than the sulfur vacancies.

These results indicate the loss of brightness observed during degradation can be attributed to the introduction of oxygen into the ZnS lattice. The dominant diffusion mechanism for oxygen in the ZnS is by hopping on sulfur vacancies, which is the most energetically favored diffusion pathway. This evidence also suggests that oxygen would preferentially occupy sulfur vacancies and form isoelectronic traps in the crystal lattice. These traps reduce the number of free carriers in the material by providing an efficient non-radiative relaxation pathway, which would result in a significantly lower activation rate for the Mn luminescent centers.
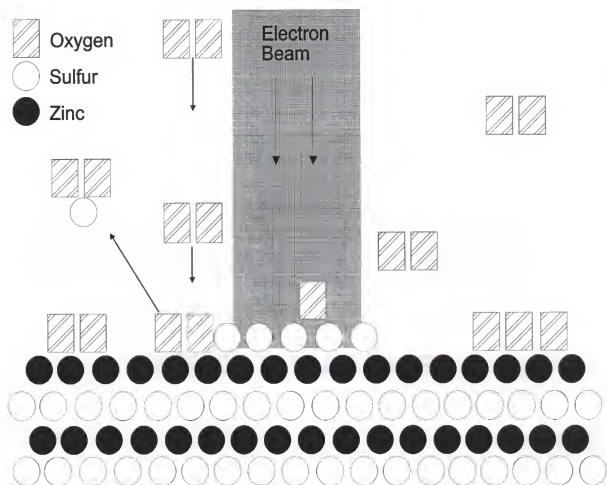
Figure 5.1.   Schematic drawing of the electron stimulated surface reaction (ESSR) process leading to degradation of CL intensity in ZnS phosphors.
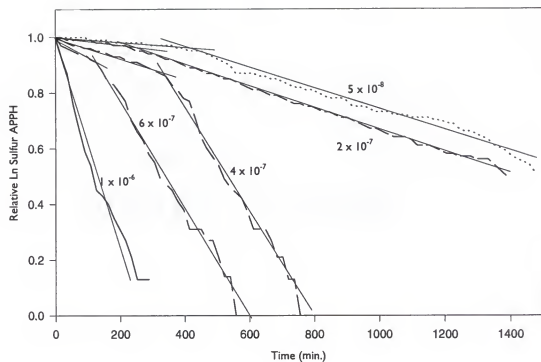
Figure 5.2.   Relative Ln sulfur APPH normalized to the value at time = 0 vs. 2 keV
electron dose for five different oxygen pressures (in Torr) measured
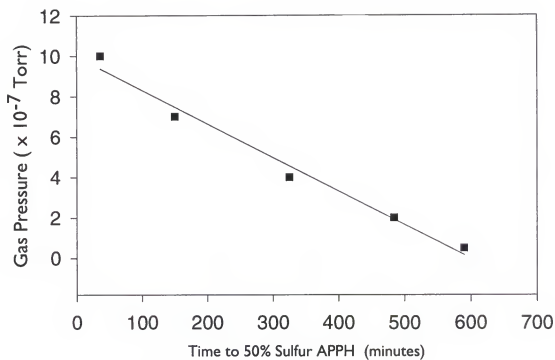at 2 keV.

Figure 5.3.   Time required to reduce the sulfur APPH to 50% of the original value
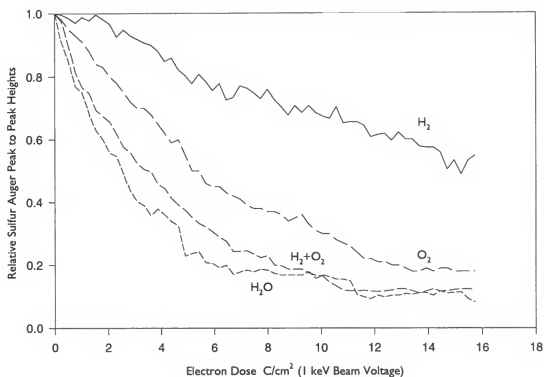vs. oxygen pressure for 2 keV electrons.

Figure 5.4.   Sulfur APPH vs. 1 keV electron dose for H_2, O_2, a 1:1 mixture of O_2 and H_2 and H_2O at 1 keV and 1×10^{-6} Torr of gas.
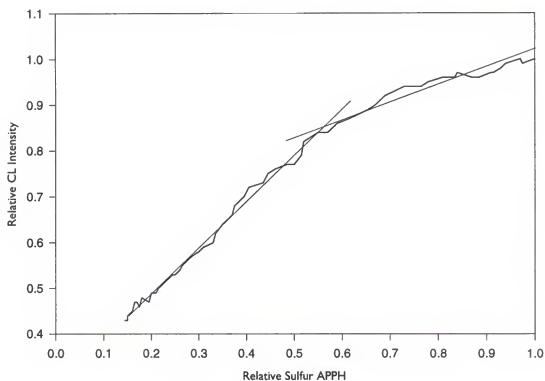
Figure 5.5.   Relative CL brightness vs. relative sulfur Auger peak-to-peak height during electron bombardment with 4 keV primary electrons in oxygen at 1 x 10⁻⁶ Torr.
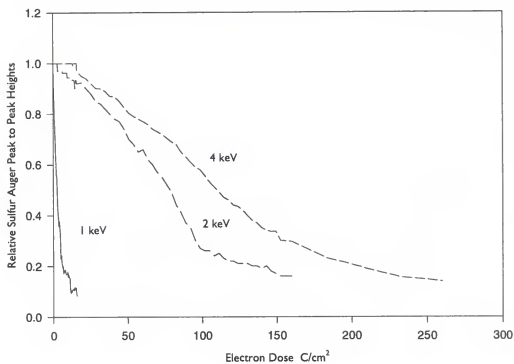
Figure 5.6.   Comparison of changes in sulfur APPH vs. electron dose during electron
               beam bombardment with 1, 2, and 4 keV primary electrons in
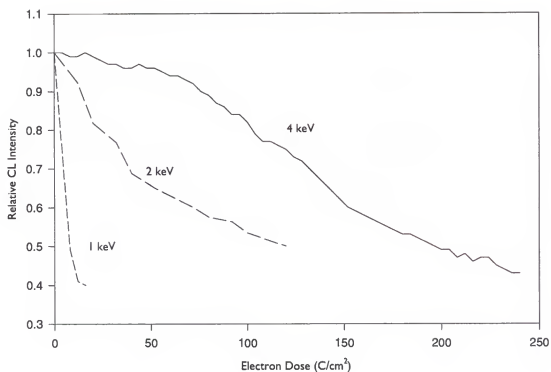 5×10^{-8} Torr water vapor.

Figure 5.7.   Comparison of changes in relative cathodoluminescent intensity vs.
electron dose during electron beam bombardment with 1, 2, and 4 keV
primary electrons in 1 x 10⁻⁶ Torr oxygen.
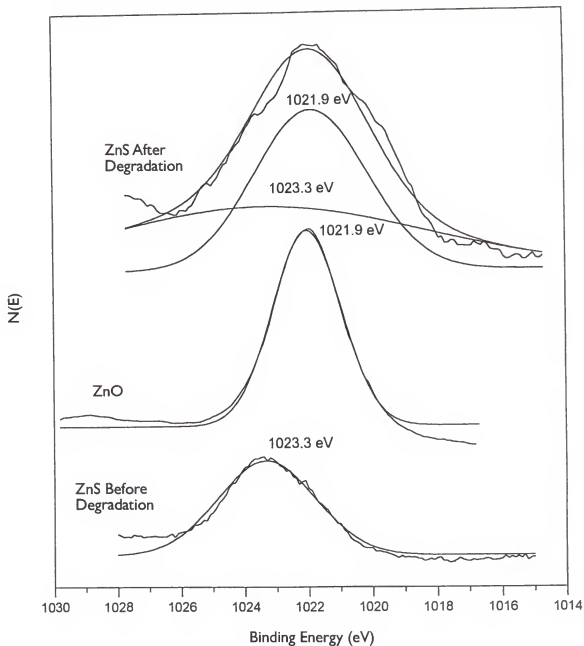
Figure 5.8.   XPS spectra of the Zn 2p peaks for ZnS before and after degradation
with a 2 keV electron beam in oxygen, and the reference ZnO sample
[Oosthuizen et al. 1997].
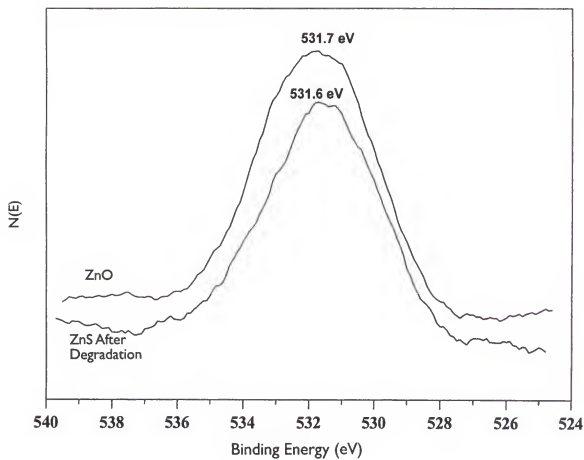
Figure 5.9.   Oxygen XPS spectra of the ZnO standard and ZnS after degradation with
2 keV electrons in oxygen [Oosthuizen 1997].
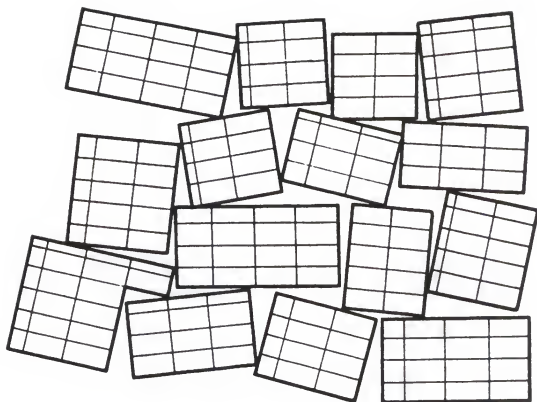
Figure 5.10. Example of the mosaic structure of a real single crystal [Cullity 1978].
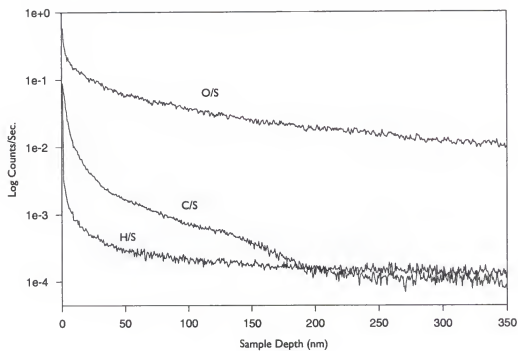
Figure 5.11.   SIMS sputter depth profile with the oxygen, carbon and hydrogen signals normalized to the matrix element, sulfur, for the reference sample.
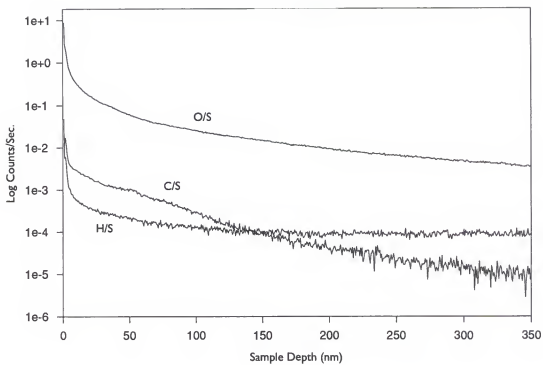
Figure 5.12. SIMS sputter depth profile with the oxygen, carbon and hydrogen signals normalized to the matrix element, sulfur, for the degraded sample.
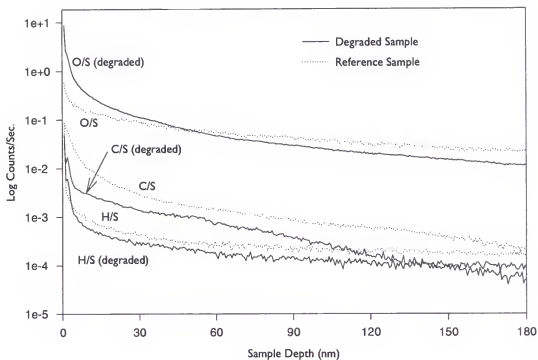
Figure 5.13. SIMS sputter depth profiles showing O/S, C/S and H/S ratios for both the reference and degraded samples.
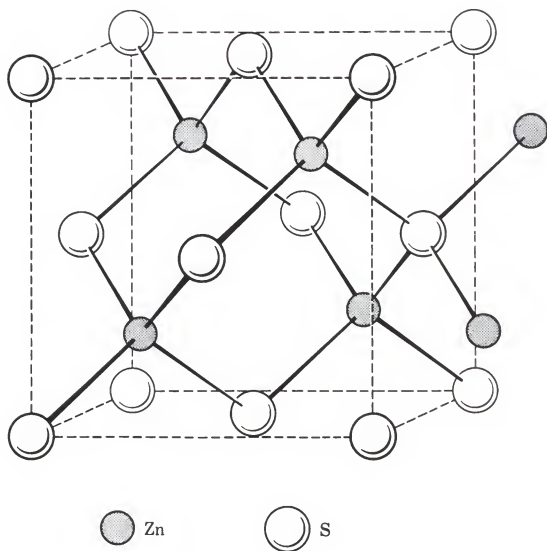
Figure 5.14. Diagram of the zinc blende (ZnS) structure [Kingery et al. 1976].
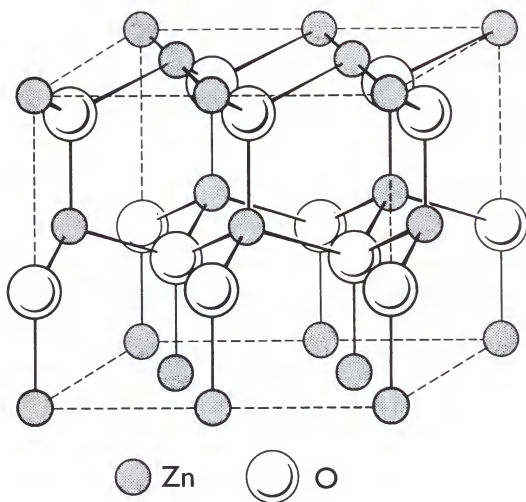
Figure 5.15.   Wurtzite structure [Kingery et al. 1976].
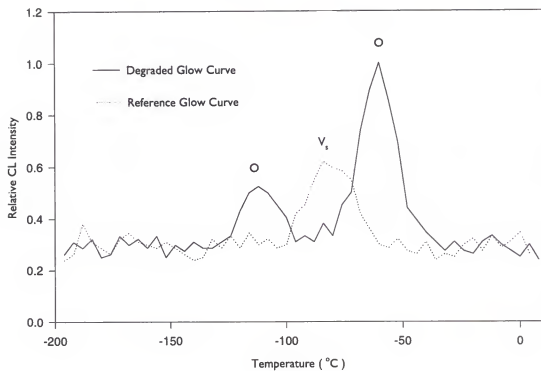
Figure 5.16.   Glow curves for both the degraded and reference samples of ZnS:Mn.

CHAPTER 6
CONCLUSIONS AND FUTURE WORK

Samples of ZnS:Mn thin films and single crystals have been subject to electron bombardment over a range of pressures from 1×10^{-6} to 5×10^{-8} Torr. Various gases including hydrogen, oxygen and water vapor were introduced into the vacuum ambient during bombardment to assess their effects on the phosphor surface. The chemical changes of the surface were monitored during degradation with Auger Electron Spectroscopy (AES) and luminescent spectrum were collected periodically with an optical spectrometer. These data indicate that electron bombardment in the presence of hydrogen, oxygen or water vapor caused depletion of sulfur from the surface of the phosphor. Concurrent increases in the oxygen and zinc APPH during bombardment in oxygen and water vapor and post degradation analysis showed the conversion of the surface from ZnS to ZnO. These phenomena are consistent with an electron stimulated surface reaction where a molecule from the vacuum ambient adsorbs on the surface of the phosphor and is dissociated to atomic species under the influence of the electron beam. These atomic species reacted with surface sulfur atoms presumably to form volatile molecules, e.g., H_2S or SO_x which have high vapor pressure and desorb from the surface depleting it of sulfur. Additional oxygen atoms then bonded with the exposed zinc atoms to form ZnO. A model has been developed to explain the ESSR reaction, and this model was demonstrated to fit the data over nearly two orders of

magnitude of gas pressure and up to 200 C/cm^2 in electron dose. The changes in surface chemistry, specifically the removal of sulfur and growth of the surface oxide, were also correlated with a reduction in cathodoluminescent (CL) brightness from the samples.

Typically, a sample degraded in oxygen would form approximately 3 nm of oxide by the time the CL brightness had been reduced to 50% of its original intensity. Three aspects of the degraded phosphor were evaluated to explain the loss of CL brightness: the oxide layer, the activator ion and the host lattice. Both the optical absorption of light and attenuation of the primary electron beam by the oxide layer were evaluated, and these factors could account for 8% of the brightness loss. The Mn^{+2} ion exhibited no change in emission spectrum during degradation which showed that the crystal field of the activator remained constant. Efficiency data collected on this ion from both as deposited and degraded samples showed a 5% change in efficiency, corresponding to a 5% loss of brightness. These results indicated the majority of the brightness loss must have resulted from changes in the host lattice, ZnS.

Single crystals of ZnS were ion implanted with Mn and annealed to produce luminescent samples. These were characterized with High Resolution X-Ray Diffraction (HRXRD) to assure the original crystal quality was recovered after implantation and anneal. X-ray maps taken both before and after sputtering with Ar$^+$ showed significant broadening, which is consistent with the incorporation of point and extended defects in the lattice by the ion bombardment. Cathodoluminescent measurements during sputter showed a significant decrease in CL brightness from the sample. These data suggest the sputter damage formed nonradiative recombination sites in the lattice. Both the

degraded and reference areas were analyzed by Secondary Ion Mass Spectrometry (SIMS), which showed significantly more oxygen in the first 51 nm of the degraded sample as compared to the reference. Thermoluminescent (glow) data established that a different trap site was formed in the phosphor after degradation. The characteristics of these traps were consistent with an oxygen atom substituting for a sulfur (or occupying a sulfur vacancy) in the lattice to form an isoelectronic electron trap. The data were interpreted to suggest that these non luminescent traps compete with the Mn^{+2} ions and reduce the carrier concentration in the host lattice, which caused the observed brightness loss in the sample.

The simplest and most effective way to avoid this degradation is to improve the vacuum ambient of the phosphor during operation. The data show measurable degradation at 1×10^{-8} Torr, while it is common for sealed field emission display (FED) devices to operate at total pressures of 1×10^{-6} Torr or higher. It should be possible with the proper design of vacuum conductance, materials selection and getter design to attain this level of vacuum for active species in a real device. This research has clearly shown the importance of reducing the partial pressure of the reactive species, especially oxygen and water vapor. Another possibility to reduce degradation would be to introduce a mechanism to transfer charge from the isoelectronic traps to the luminescent ion. The addition of Yb^{3+} or Eu^{3+} to the $Y_3(Al, Ga)_5O_{12}$:Tb phosphor system has been demonstrated to reduce the effects of ageing during electron bombardment under CRT conditions [Matsukiuo et al.]. These authors assert that the origin of ageing in the original sample was due to the formation of electron traps which they demonstrated using glow experiments. Their results

suggest that these additional ions also trap electrons, competing with the non radiative traps in the phosphor [Matsukiuo et al. 1991], and transfer charge to luminescent centers. It would be interesting to determine if a dopant ion could be incorporated that would have a similar effect in the ZnS:Mn phosphor system.

APPENDIX A
OPTICAL ABSORPTION CALCULATIONS

In order to calculate the optical absorption in the ZnO surface layer a reference ZnO sample was measured for optical absorption. This sample was a 414 nm layer of ZnO deposited on a silica substrate. At 550 nm the sample absorbed 62% of the light from the source. The relationship between the light absorbance and the thickness of a material is given by [Hummel 1985]:

$$I = Io \cdot exp\left(-2 \cdot \omega \cdot k \cdot \frac{z}{c}\right) \qquad A.1$$

where I is the transmitted intensity, Io is the original intensity, c is the velocity of light, z is the thickness of the absorbing layer, k is the (unitless) damping constant and ω is the angular frequency given by:

$$\omega = \frac{2 \cdot c \cdot \pi}{\lambda} \qquad A.2$$

where λ is the wavelength of the light. At 550 nm:

$$\omega = 3.427 \cdot 10^{15} \cdot sec^{-1}$$

Solving equation A.1 for k yields:

$$k = -\frac{1}{2} \cdot \frac{ln\left(\frac{I}{Io}\right)}{(\omega \cdot z)} \cdot c \qquad A.3$$

155

For the reference sample I=.38, Io=1, and z is 414 nm. By substituting these values into

A.3:

$$k = 0.102$$

and using this damping constant for the sample thickness (3 nm) gives an absorbance of

0.7% (I=0.993) in the ZnO layer at 550 nm.

REFERENCES

[Alexander 1995]   Alexander W.B., Ph.D. dissertation, University of Florida, Gainesville, FL, 1995.

[Allen 1971]   Allen J.W., *Journal of Physics*, **C4**, 1936, 1971.

[Animalu 1966]   Animalu A.O.E., *Proceedings of the Royal Society of London*, **294**, 376, 1966.

[Aten et al. 1965]   Aten A.C., J.H. Haanstra and H. de Vries, *Philips Research Reports*, **20**, 395, 1965.

[Atkins 1990]   Atkins P.W., *Physical Chemistry*, **4**, Oxford University Press, Oxford, 1990.

[Auth and Ridder 1957]   Auth J. and R. Ridder, *Annals of Physics*, **20**, 210, 1957.

[Baldereschi 1973]   Baldereschi A., *Journal of Luminescence*, **7**, 79, 1973.

[Baldereschi and Hopefield 1972]   Baldereschi A. and J.J. Hopefield, *Physical Review Letters*, **28**, 171, 1972.

[Balkanski et al. 1966]   Balkanski M., R. Beserman and D. Langer, *Proceedings of the International Conference on Luminescence*, 1186, Berlin, 1966.

[Bartels 1983]   Bartels W.J., *Journal of Vacuum Science and Technology B*, **1**, 338, 1983.

[Benny and Morten 1958]   Benny A.H. and F.D. Morten, *Proceedings of the Physical Society of London*, **72**, 1007, 1958.

[Bethe and Ashkin 1953]   Bethe H.A. and J. Ashkin, *Experimental Nuclear Physics*, Wiley and Sons, New York, 1953.

[Bechtel et al. 1996]   Bechtel H., W. Czarnohan, M. Haase and D. Wadow, *Journal of the Society for Information Display*, **4/3**, 219, 1996.

157

[Benninghoven et al. 1987]   Benninghoven A., F.G. Rudenauer and H.W. Werner, *Secondary Ion Mass Spectrometry Basic Concepts, Insturmental Aspects, Applications and Trends*, Wiley and Sons, New York, 1987.

[Blasse and Grabmaier 1994]   Blasse G. and B.C. Grabmaier, *Luminescent Materials*, Springer-Verlag, 1, New York, 1994.

[Bril 1954]   Bril A., *British Journal of Applied Physics Suppliment*, 4, 10, 1954.

[Bril and Klasens 1952]   Bril A. and H.A. Klasens, *Philips Research Reports*, 7, 401, 1952.

[Brody 1973]   Brody P., *IEEE Transactions on Electron Devices*, **ED20**, 995, 1973.

[Broser and Broser 1958]   Broser I. and R. Broser, *Journal of the Physics and Chemistry of Solids*, 6, 386, 1958.

[Brumage et al. 1964]   Brumage W.A., C.R. Yarger and C.C. Lin, *Physical Review*, **133 A**, 765, 1964.

[Brundle et al. 1992]   Brundle C.R., C.A. Evans and S. Wilson, *Encyclopedia of Materials Characterization*, Butterworth-Heinemann, Boston, 1992.

[Bryant and Hamid 1970]   Bryant F.J. and S.A. Hamid, *Physica Status Solidi*, 2, 597, 1970.

[Bryant and Manning 1972]   Bryant F.J. and P.S. Manning, *Radiation Effects*, 13, 267, 1972.

[Coburn 1968]   Coburn J.W., *Surface Science*, 11, 61, 1968.

[Cotton 1990]   Cotton F.A., *Chemical Applications of Group Theory*, 3rd ed., Wiley, Chichesterter England, 1990.

[Cullity 1978]   Cullity B.D., *Elements of X-Ray Diffraction*, 2nd ed., Addison-Wesley, Reading MA, 1978.

[Curtin 1991]   Curtin C., *Proceedings of the 1991 International Display Research Conference*, IEEE, 12, 1991.

[Darici and Holloway 1997]   Darici Y., and P. H. Holloway, *Journal of Vacuum Science and Technology*, In Press.

[Davis et al. 1976] Davis L.E., N.C. McDonald, P.W. Palmberg, G.E. Riach and R.E. Weber, *Handbook of Auger Electron Spectroscopy*, 2nd ed., Physical Electronics Division Perkin-Elmer Corp., Eden Prarie, MN, 1976.

[DiBartolo 1968] DiBartolo B., *Optical Interactions in Solids*, Wiley, New York, 1968.

[Diemer et al. 1958] Diemer G., G.J van Gurp, and W. Hoogenstraaten, *Philips Research Reports*, **13**, 458, 1958.

[Doane 1995] Doane J.W., *Flat-Panel Display Technologies*, L.E. Tannas, W.E. Glenn and J.W. Doane ed., Noyes, New Jersey, 1995.

[Dowling and Sewell 1953] Dowling P.H. and J.R. Sewell, *Journal of the Electrochemical Society*, **100**, 22, 1953.

[Feldman 1960] Feldman C., *Physical Review*, **117**, 455, 1960.

[Garlick 1966] Garlick G.F.G., *Luminescence of Inorganic Solids*, P. Goldberg ed., Academic Press, New York, 1966.

[Garlick et al. 1949] Garlick G.F.G., A.F. Wells and M.H.F. Wilkins, *Journal of Chemical Physics*, **17**, 399, 1949.

[Gergely 1959] Gergely G., *Physical Chemistry*, **211**, 274, 1959.

[Gergely 1960] Gergely G., *Journal of the Physics and Chemistry of Solids*, **17**, 112, 1960.

[Harten 1959] Harten H.U., *Philips Research Reports*, **14**, 346, 1959.

[Hase et al. 1990] Hase T., T. Kano, E. Nakazawa, H. Yamamoto, *Advances in Electronics and Electron Physics*, P. W. Hawkes ed., **79**, Academic, New York, 1990.

[He and Razeghi 1993] He X. and M. Razeghi, *Journal of Applied Physics*, **73**, 3284, 1993.

[Heinke et al. 1994] Heinke H., M.O. Moller, D. Hommel and G. Landwehr, Journal of Crystal Growth, **135**, 41, 1994.

[Henderson and Imbusch 1989] Henderson B. and G.F. Imbusch, *Optical Spectroscopy of Inorganic Solids*, Clarendon, Oxford, 1989.

[Holloway 1980]   Holloway P.H., *Advances in Electronics and Electron Physics*, **54**, 241, 1980.

[Holloway et al. 1994]   Holloway P.H., J.E. Yu, P. Rack, J. Sebastian, S. Jones, T. Trottier, K.S. Jones, B. Pathangey, T.J. Anderson, S.S. Sun, R. Tuenge, E. Dickey and C.N. King, *Materials Research Society Symposium Proceedings*, **345**, 289, 1994.

[Hoogenstraaten 1958]   Hoogenstraaten W., *Phillips Research Reports*, **13**, 515, 1958.

[Hopefield et al. 1966]   Hopefield J.J., D. G. Thomas and R.T. Lynch, *Physical Review Letters*, **17**, 312, 1966.

[Hughes 1969]   Hughes H.L., *IEEE Transactions on Nuclear Science*, **NS-16**, 195, 1969.

[Hummel 1985]   Hummel R.E., *Electronic Properties of Materials*, Springer-Verlag, New York, 1985.

[Itoh et al. 1989]   Itoh S., T. Kimizuka and T.Tonegawa, *Journal of the Electrochemical Society*, **136**, 1819, 1989.

[Johnson 1939]   Johnson R.P., *Journal of the Optical Society of America*, **29**, 187, 1939.

[Johnson and Williams 1950a]   Johnson P.D. and F.E. Williams, *Journal of Chemistry and Physics*, **18**, 323, 1950.

[Johnson and Williams 1950b]   Johnson P.D. and F.E. Williams, *Journal of Chemistry and Physics*, **18**, 1477, 1950.

[Kalkhoran et al. 1994]   Kalkhoran N., K., H.P. Maruska and F. Namavar, *Materials Research Society Symposium Proceedings*, **316**, 481, 1994.

[Kaminski 1965]   Kaminski M., *Atomic and Ionic Impact on Metal Surfaces*, Academic Press, New York, 1965.

[Kingery et al. 1976]   Kingery W.D., H.K. Bowen and D.R. Uhlmann, *Introduction to Ceramics*, 2nd edition, Wiley & Sons, New York, 1976.

[Kingsley and Prener 1972]   Kingsley J.D. and J. S. Prener, *Journal of Applied Physics*, **43(7)**, 3073, 1972.

[Klaassen and Leeuw 1987]   Klaassen D.B.M. and D.M. de Leeuw, *Journal of Luminescence*, **37**, 21, 1987.

[Klasens 1946]   Klasens H.A., *Nature*, **158**, 306, 1946.

[Klasens 1958]   Klasens H.A., *Journal of the Physics and Chemistry of Solids*, **7**, 175, 1958.

[Klein 1968]   Klein C.A., *Journal of Applied Physics*, **39**, 2029, 1968.

[Kroeger 1948]   Kroeger F.A., *Some Aspects of the Luminescence of Solids*, Elsevier, New York, 1948.

[Kroeger and Dikhoff 1952]   Kroeger F.A. and J.A.M. Dikhoff, *Phillips Research Laboratory Reports*, **99(4)**, 144, 1952.

[Leeuw and Hooft 1983]   Leeuw D.M. and G.W. 't Hooft, *Journal of Luminescence*, **28**, 275, 1983.

[Leutwein et al. 1967]   Leutwin K., A. Rauber and J. Schnider, *Solid State Communications*, **5**, 783, 1967.

[Ludwig and Kingsley 1970]   Ludwig G.W. and J.D. Kingsley, *Journal of the Electrochemical Society*, **117(3)**, 348, 1970.

[Madey and Yates 1971]   Madey T.E. and J.T. Yates, *Journal of Vacuum Science and Technology*, **8(4)**, 525, 1971.

[Makhov 1961]   Makhov A.F., *Soviet Physics Solid State*, **2**, 1934, 1961.

[Massey and Burhop 1952]   Massey H. and E. Burhop, *Electronic and Ionic Impact Phenomena, Oxford*, London England, 1952.

[Matsueda 1989]   Matsueda Y., *Society for Information Display 1989 Digest of Technical Papers*, 238, San Diego Ca, 1989.

[Matsukiyo et al. 1991]   Matsukiyo H., T. Suzuki, and H.Yamada, *Electrochemical Society Meeting Extended Abstracts*, **91-2**, 965, 1991.

[McClure 1963]   McClure D.S., *Journal of Chemistry and Physics*, **39**, 2850, 1963.

[Menzel and Gomer 1964]   Menzel D. and R. Gomer, *Journal of Chemistry and Physics*, **41**, 3329, 1964.

[Mikoshiba 1993]   Mikoshiba S., Plasma Displays, *Proceedings of the Society for Information Display Seminar*, F-2, Boston MA, 1993.

[Moore 1961]   Moore G.E., *Journal of Applied Physics*, **32**, 1241, 1961.

[Morimoto 1982]   Morimoto K., *Society For Information Display International Symposium on Digital Technology Papers XIII*, 218, 1982.

[Nail et al. 1949]   Nail N.R., F. Urbach and D. Pearlman, *Journal of the Optical Sociey of America*, **39**, 690, 1949.

[Nakajima et al. 1989]   Nakajima H., *Society for Information Display 1989 Digest of Technical Papers*, 234, San Diego CA, 1989.

[Nefedov 1982]   Nefedov V.I., *Journal of Electron Spectroscopy and Related Phenomena*, **25**, 29, 1982.

[Nishihima and Propst 1970]   Nishihima M. and F.M. Propst, *Physical Review*, **B2**, 2368, 1970.

[O'Hanlon 1989]   O'Hanlon J.F., *A Users Guide to Vacuum Technology*, 2nd ed., Wiley & Sons, New York, 1989.

[Ohuchi and Holloway 1982]   Ohuchi F. and P. Holloway, *Journal of Vacuum Science and Technology*, **20(3)**, 863, 1982.

[Oosthuizen et al. 1997]   Oosthuizen L., Swart H., P. Viljoen, P. Holloway and G. Berning, *Applied Surface Science*, In Press.

[Ozawa 1990]   Ozawa L., *Cathodoluminescence Theory and Applications*, VCH Publishers, New York, 1990.

[Ozawa et al. 1966]   Ozawa L., R. Huzimaura and Y. Ato, *Proceedings of the International Conference on Luminescence*, 1177, Berlin, 1966.

[Pankove 1971]   Pankove J.I., *Optical Processes in Semiconductors*, Dover, New York, 1971.

[Petrovich 1995]   Petrovich T., *Electronic Design*, **1**, 95, 1995.

[Pfahnl 1961]   Pfahnl A., *Advances in Electron Tube Techniques*, Pergamon Press, New York, 204, 1961.

[Phillips 1969]   Phillips J.C., *Physical Review Letters*, **22**, 285, 1969.

[Randall and Wilkins 1945]   Randall J.T. and M.H.F. Wilkins, *Proceedings of the Royal Society A*, **184**, 366, 1945.

[Redhead 1964]   Redhead P.A., *Canadian Journal of Physics*, **42**, 886, 1964.

[Redhead et al. 1968]   P.A. Readhead, J.P. Hobson and E.V. Kornelsen, *The Physical Basis of Ultrahigh Vacuum*, Chapman and Hall LTD, London, 1968.

[Roberts 1957]   Roberts S., *Journal of Applied Physics*, **28**, 262, 1957.

[Roberts and Williams 1950]   Roberts S. and F.E. Williams, *Journal of the Optical Society of America*, **40**, 516, 1950.

[Robbins 1980]   Robbins D.J., *Journal of the Electrochemical Society*, **127**, 2694, 1980.

[Schon 1952]   Schon M., *Zhurnal Physik*, **119**, 483, 1942.

[Schon 1954]   Schon M., *Physica*, **20**, 930, 1954.

[Sebastian et al. 1997]   Sebastian J., H. Swart, T. Trottier, S. Jones and P. Holloway, *Journal of Vacuum Science and Technology A*, **15(4)**, 2394, 1997.

[Seiwert 1949]   Seiwert R., *Annals of Physics*, **6**, 241, 1949.

[Shalimova et al. 1976]   Shalimova K., N. Morozova, O. Korolev, M. Veselkova, I. Karethnikov and B. Kurbatov, *Journal of Applied Spectroscopy*, **24**, 1274, 1976.

[Smith 1948]   Smith A.L., *Journal of the Electrochemical Society*, **93**, 324, 1948.

[Smith and Turkevich 1954]   Smith A.W. and J. Turkevick, *Physical Review*, **94**, 895, 1954.

[Spencer 1955]   Spencer L.V., *Physical Review*, **98**, 1597, 1955.

[Spindt 1968]   Spindt C.A., *Journal of Applied Physics*, **39**, 3504, 1968.

[Swart et al. 1996]   Swart H.C., J.S. Sebastian, T.A. Trottier, S.L. Jones and P.H. Holloway, *Journal of Vacuum Science and Technology*, **14(3)**, 1697, 1996.

[Swart et al. 1997]   Swart H.C., T.A. Trottier, J.S. Sebastian, S.L. Jones and
                        P.H. Holloway, *Journal of Vacuum Science and Technology*, In
                        Press, 1997.

[Sze 1981]   Sze, S.M., *Physics of Semiconductor Devices*, 2nd ed., Wiley, New York,
               1981.

[Thomas et al. 1965]   Thomas D.G., J.J. Hopefield and C.J. Frosch, *Physical
                         Review Letters* **15**, 857, 1965.

[Tomozawa and Doremus 1979]   M. Tomozawa and R. H. Doremus, *Treatise on
                                Materials Science and Technology*, Academic Press,
                                New York, 1979.

[Trumbore et al. 1966]   Trumbore F.A., M. Gershenzon and D.G. Thomas, *Applied
                           Physics Letters*, **9**, 4, 1966.

[Vechten and Phillips 1970]   Vechten J.A. and J.C. Phillips, *Physical Review*, **B2**,
                                2160, 1970.

[Wang 1950]   Wang T.J., *Nucleonics*, **7(2)**, 55, 1950.

[Williams and de Segovia 1989]   Williams E.M. and J.L. de Segovia, *Vacuum*, **39**, 633,
                                   1989.

[Wu et al. 1982]   Wu C., Y. Zhu and Z. Chen, *Journal of Vacuum Science and
                     Technology* , **20(4)**, 1034, 1982.

[Yu 1994]   Yu J.E., Ph.D. dissertation, University of Florida, Gainesville
              FL, 1994.

BIOGRAPHICAL SKETCH

Joseph Samuel Sebastian was born in 1967 in Evanston, IL. When he was two, his family relocated to Cincinnati, OH, where Joseph spent his formative years and attended Turpin High School. Upon graduation he entered Ohio State University and had the honor of initiation into the Sigma Chi fraternity. His passion for climbing and mountaineering developed during this time, and he spent countless weekends and breaks enjoying these interests. After receiving a B.S. in ceramic engineering in 1991, Joseph earned a PADI dive master certification and traveled to Key West, Fl, where he spent a year working as a dive master. In 1992 Joseph entered the Materials Science and Engineering department at the University of Florida, and received funding from the International Society for Hybrid Microelectronics for his work on high temperature solid oxide fuel cells. During this period, he was inducted into the engineering honors society, Tau Beta Pi. After joining Dr. Paul Holloway's research group, his focus shifted to luminescent materials within the newly formed Phosphor Technology Center of Excellence. After managing Dr. Holloway's lab for two years, Joseph will graduate in August of 1997 with a Ph.D. in materials science. An avid sailor, he plans to spend time in the Caribbean aboard his sailboat, Raven, before joining Intel at their microprocessor development facility in Portland, OR, as a senior process engineer.

I certify that I have read this study and that in my opinion it conforms to acceptable standards of scholarly presentation and is fully adequate, in scope and quality, as a dissertation for the degree of Doctor of Philosophy.
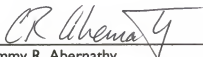
Paul H. Holloway
Professor of Materials Science
and Engineering

I certify that I have read this study and that in my opinion it conforms to acceptable standards of scholarly presentation and is fully adequate, in scope and quality, as a dissertation for the degree of Doctor of Philosophy.

Rolf E. Hummel
Professor of Materials Science
and Engineering

I certify that I have read this study and that in my opinion it conforms to acceptable standards of scholarly presentation and is fully adequate, in scope and quality, as a dissertation for the degree of Doctor of Philosophy.

Cammy R. Abernathy
Professor of Materials Science
and Engineering

I certify that I have read this study and that in my opinion it conforms to acceptable standards of scholarly presentation and is fully adequate, in scope and quality, as a dissertation for the degree of Doctor of Philosophy.

Kevin S. Jones
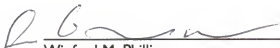Associate Professor of Materials Science
and Engineering

I certify that I have read this study and that in my opinion it conforms to acceptable standards of scholarly presentation and is fully adequate, in scope and quality, as a dissertation for the degree of Doctor of Philosophy.

David B. Tanner
Professor of Physics

This dissertation was submitted to the Graduate Faculty of the College of Engineering and to the Graduate School and was accepted as partial fulfillment of the requirements for the degree of Doctor of Philosophy.

August, 1997

Winfred M. Phillips
Dean, College of Engineering

Karen A. Holbrook
Dean, Graduate School